

Proton Beam Energy Requirements for LBNE

Mary Bishai¹, Milind Diwan¹, Yi Lu², Lisa Whitehead¹

¹ *Brookhaven National Lab, Upton, NY 11973, USA*

² *Manhasset High School, Manhasset, NY, USA*

Abstract

Recent LBNE sensitivity studies have indicated that boosting the neutrino flux around 1 GeV can significantly improve the sensitivity to the mass hierarchy and CP violation. Reducing the primary proton beam energy is one of the most promising options for boosting pion production in the range 1-3 GeV which produces neutrinos in the range 0.4-1.2 GeV. We studied the pion production efficiency from various target materials as a function of primary proton beam energy using FLUKA08. The maximum pion production per proton-GeV for pions with momentum from 1 to 3 GeV was obtained from a graphite target with an incident proton beam energy of 10 GeV. The maximum pion production in the range of 3 to 10 GeV - which produces neutrinos at the 1st oscillation maxima was obtained from a graphite target with a 40 GeV proton beam. To boost the production of pions in the 1-3 GeV region with incident proton beam energies > 20 GeV requires the use of high-Z or hybrid low-Z/high-Z targets. **For pions in the range 0-10 GeV, the optimal pion production is at proton beam energies of < 60 GeV for all the materials studied.** A preliminary analysis of the $\nu_\mu \rightarrow \nu_e$ appearance signal and backgrounds at Homestake using a graphite target and the NuMI focusing system indicates that the best signal yield and signal to background is obtained with a primary proton beam energy of 50-60 GeV.

Contents

1	Introduction and Motivation	3
1.1	LBNE Sensitivity Beam Flux Dependence	6
2	Optimization of Pion Production	11
2.1	Pion Production and Target Material	13
2.2	Pion Production vs Proton Beam Energy	14
2.3	Summary and Discussion	20
3	Neutrino Production	22
3.1	Neutrino Production and Primary Proton Beam Energy	22
4	Physics Sensitivity Studies	27
5	Summary and Conclusions	30
	List of Tables	31
	List of Figures	31
A	Energy Deposition	35
A.1	Target	35
A.2	Decay Pipe Shielding	40
B	FNAL MI Beam Power vs Energy	47
C	BNL-AGS vs FNAL-MI LBNE Beams	48

1 Introduction and Motivation

The core long baseline physics program at LBNE focuses on observing the oscillation of $\nu_\mu \rightarrow \nu_e$. The oscillation probability depends on several unknown neutrino mixing parameters, the angle θ_{13} , the mass hierarchy of the 1 and 3 states, and the CP phase for 3 generation mixing : δ_{cp} . In Figures 1 and 2 the oscillation probability at a baseline of 1300km with different values of the unknown oscillation parameters is shown as colored curves. The unoscillated CC ν_μ spectrum from an LBNE candidate beam is shown as the solid black histogram. From these figures it is clear that the effect of the phase, δ_{cp} , is largest for neutrinos with $E_\nu < 1$ GeV. The effect of the mass hierarchy is largest for neutrinos from 2-5 GeV. The oscillation probability is small for $E_\nu > 5$ GeV. The charged-current unoscillated ν_μ spectrum at the far detector from the Aug 2010 LBNE beam designs using a 120 GeV beam from the Main Injector is shown as the black histogram in Figures 1 and 2. The 120 GeV MI LBNE beams provide excellent coverage for neutrinos > 2 GeV, but have very little flux in the region where the CP effects are largest. The goal of this report is to provide a comprehensive study of the impact of the primary proton beam energy on the LBNE neutrino flux and the physics sensitivities.

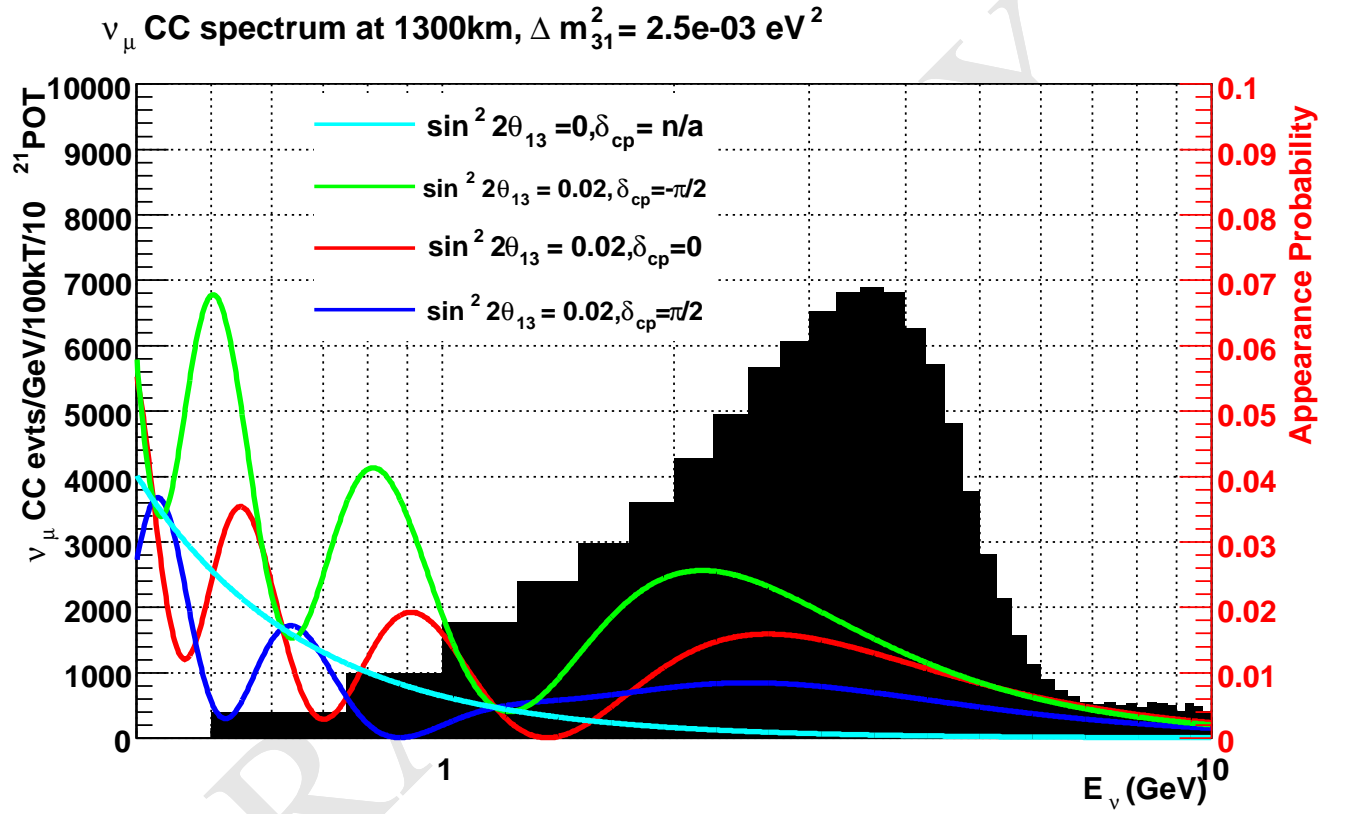


Figure 1: The $\nu_\mu \rightarrow \nu_e$ oscillation probability for the LBNE to DUSEL baseline of 1300 km for different mixing parameter with normal hierarchy is shown as colored curves. The unoscillated CC ν_μ spectrum from an LBNE candidate beam is shown as the solid black histogram.

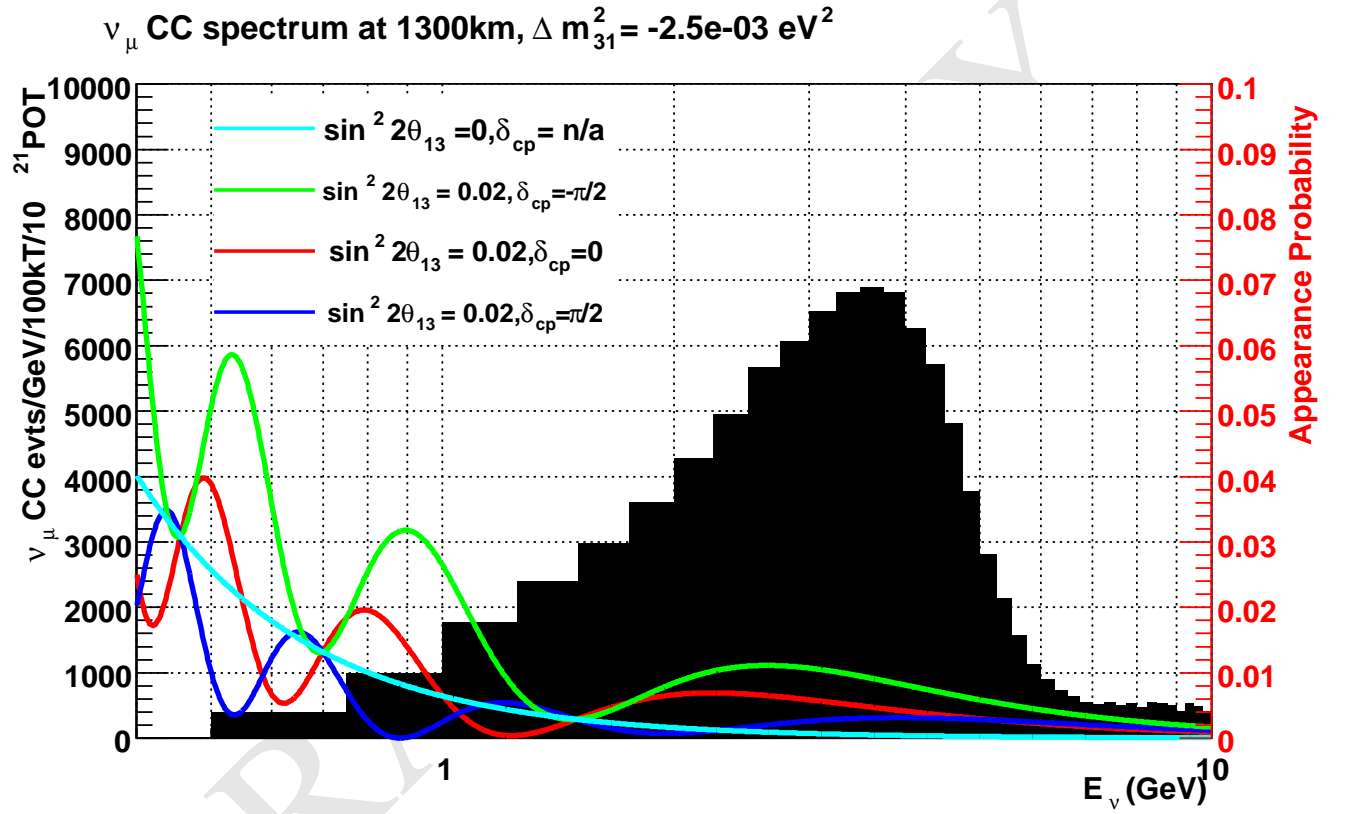


Figure 2: The $\nu_\mu \rightarrow \nu_e$ oscillation probability for the LBNE to DUSEL baseline of 1300 km for different mixing parameter with inverted hierarchy is shown as colored curves. The unoscillated CC ν_μ spectrum from an LBNE candidate beam is shown as the solid black histogram.

1.1 LBNE Sensitivity Beam Flux Dependence

There has been a lot of confusing results recently on the impact of the low energy neutrino flux in the physics sensitivity of LBNE. A recent study by Debadrata Mohapatra reported in LBNE-doc-2683 has reinforced the importance of a wide-band LOW-ENERGY beam to the measurement of CP violation and the mass hierarchy. In his study, Debadrata compared the sensitivity to θ_{13} , the mass hierarchy and CP violation using 4 different beam designs shown in Figure 3 and summarized in Table 1.

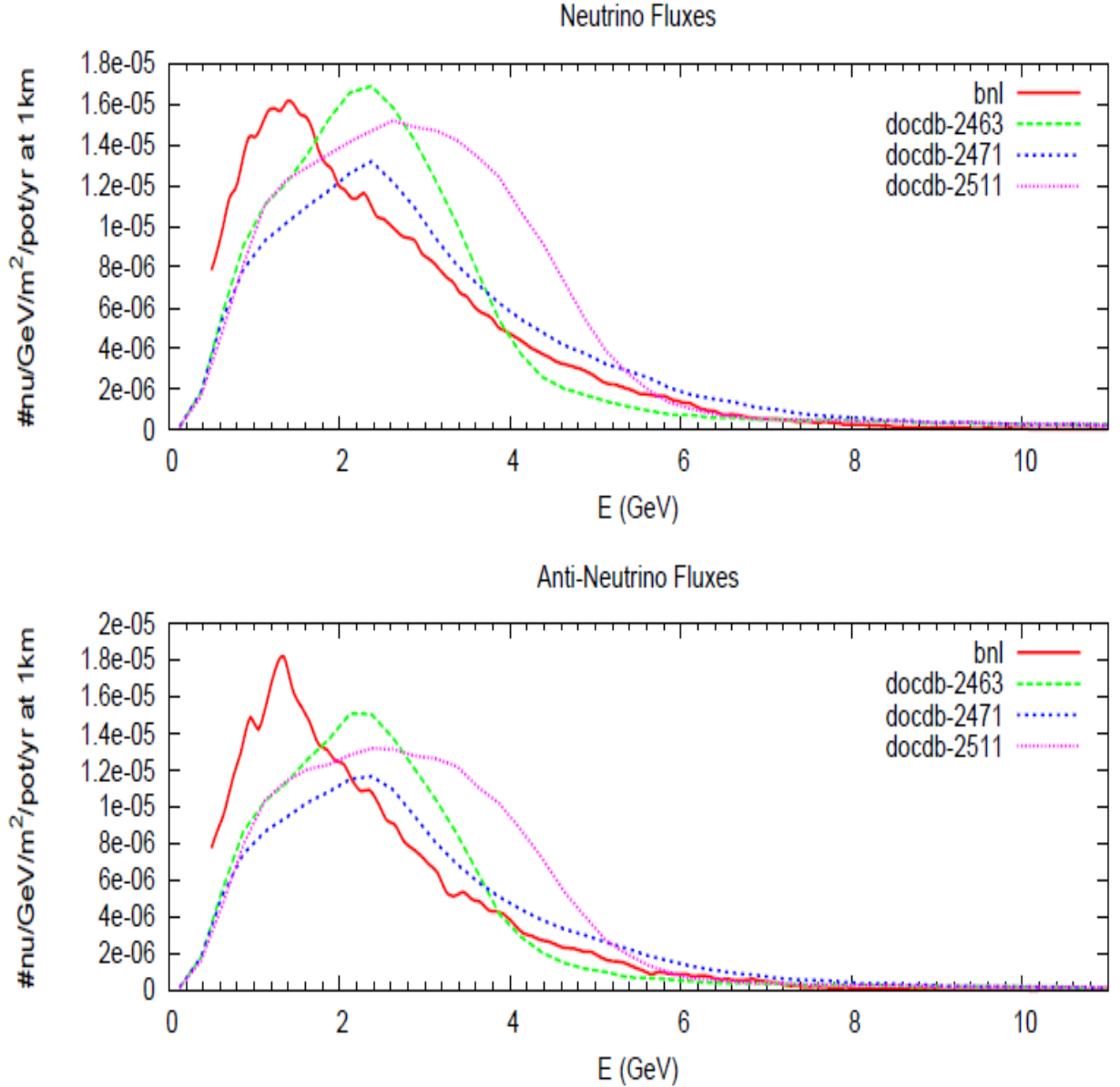


Figure 3: The ν_μ and $\bar{\nu}_\mu$ fluxes at DUSEL from different candidate beams. The AGS 28 GeV beam (red), the 2009 LBNE 120 GeV beam, the LBNE CDR beam (blue dashed line), the Aug 2010 LBNE 120 GeV beam (magenta dashed line). (D. Mohapatra, LBNE-doc-2683)

It is very clear from these preliminary studies that the 28 GeV AGS beam designs significantly outperforms all 120 GeV MI beams in the sensitivity to the mass hierarchy. In addition,

the 28 GeV AGS beam also has the best sensitivity to CP violation. The Aug 2009 120 GeV MI beam has the best θ_{13} sensitivity for most values of δ_{cp} . The Aug 2009 beam has the largest ν_e appearance rate of any of the other beams studied and we expect the overall rate to drive sensitivity to θ_{13} .

In this report we will study in detail the impact that the primary proton beam energy has on the flux and physics sensitivity of LBNE.

Table 1: Conventional neutrino 2-horn beam designs used in the sensitivity studies of LBNE-doc-2683. The BNL-AGS far detector neutrino flux used in this study was produced using the flux at the near detector scaled by $1/L^2$. The FNAL-MI fluxes are all from a FLUKA08/GEANT 3.21 simulation and are extrapolated properly to the far detector. All simulations use a cylindrical graphite target of 2 interaction lengths long with radius = 0.6 to 0.75 cm either partially (Aug 2010 flux) or wholly inserted in the the first horn.

Flux name	Doc #	Description
BNL	N/A	AGS 28 GeV beam, BNL-E734/E889 horns, 2m radius, 180m decay pipe (He)
2009 design	2463	MI 120 GeV beam, NuMI horns, 2m radius, 280m decay pipe (vacuum)
Aug 2010	2511	MI 120 GeV beam, NuMI horns, 2m radius, 280m decay pipe (vacuum)
CDR 2010	2471	MI 120 GeV beam with CDR horns, 2m radius, 250m decay pipe (air)

The physics sensitivities obtained using these 4 different fluxes with a parameterized water Cerenkov detector response are shown in Figures 4 to 6. A detector mass of 200kT fiducial is assumed and beam power of 700 kW running for 5 yrs in ν mode and 5 yrs in $\bar{\nu}$ mode. The curves indicate the sensitivity at the 3σ level.

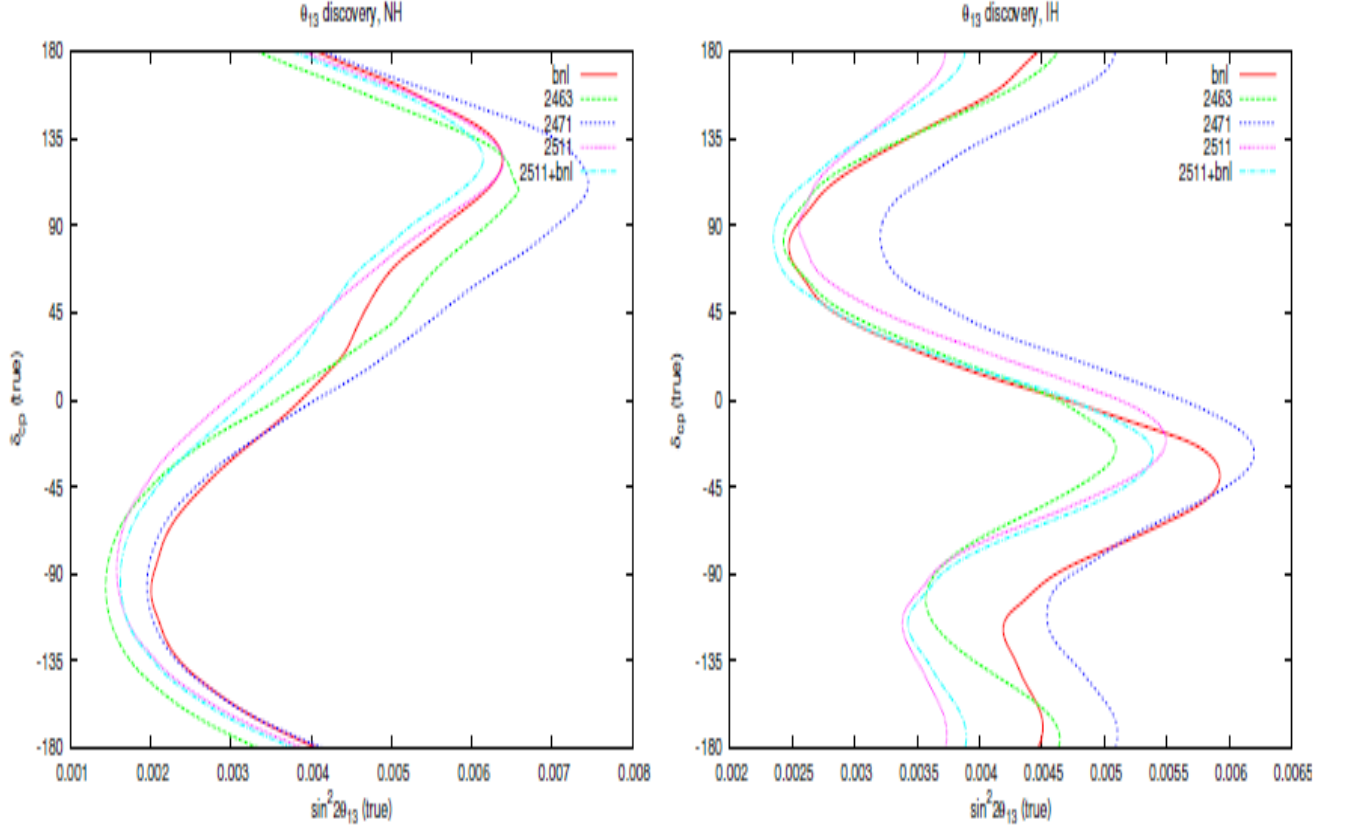


Figure 4: Physics sensitivities to non-zero θ_{13} obtained from different candidate beams using a 200kT water Cerenkov detector at DUSEL with 5 yrs ν + 5yrs $\bar{\nu}$ running. The AGS 28 GeV beam at 700kW (red), the 2009 LBNE 120 GeV beam at 700kW (green dashed line), the LBNE Sep 2010 120 GeV CDR beam (blue dashed line), the Aug 2010 LBNE 120 GeV beam (magenta dashed line). (D. Mohapatra, LBNE-doc-2683).

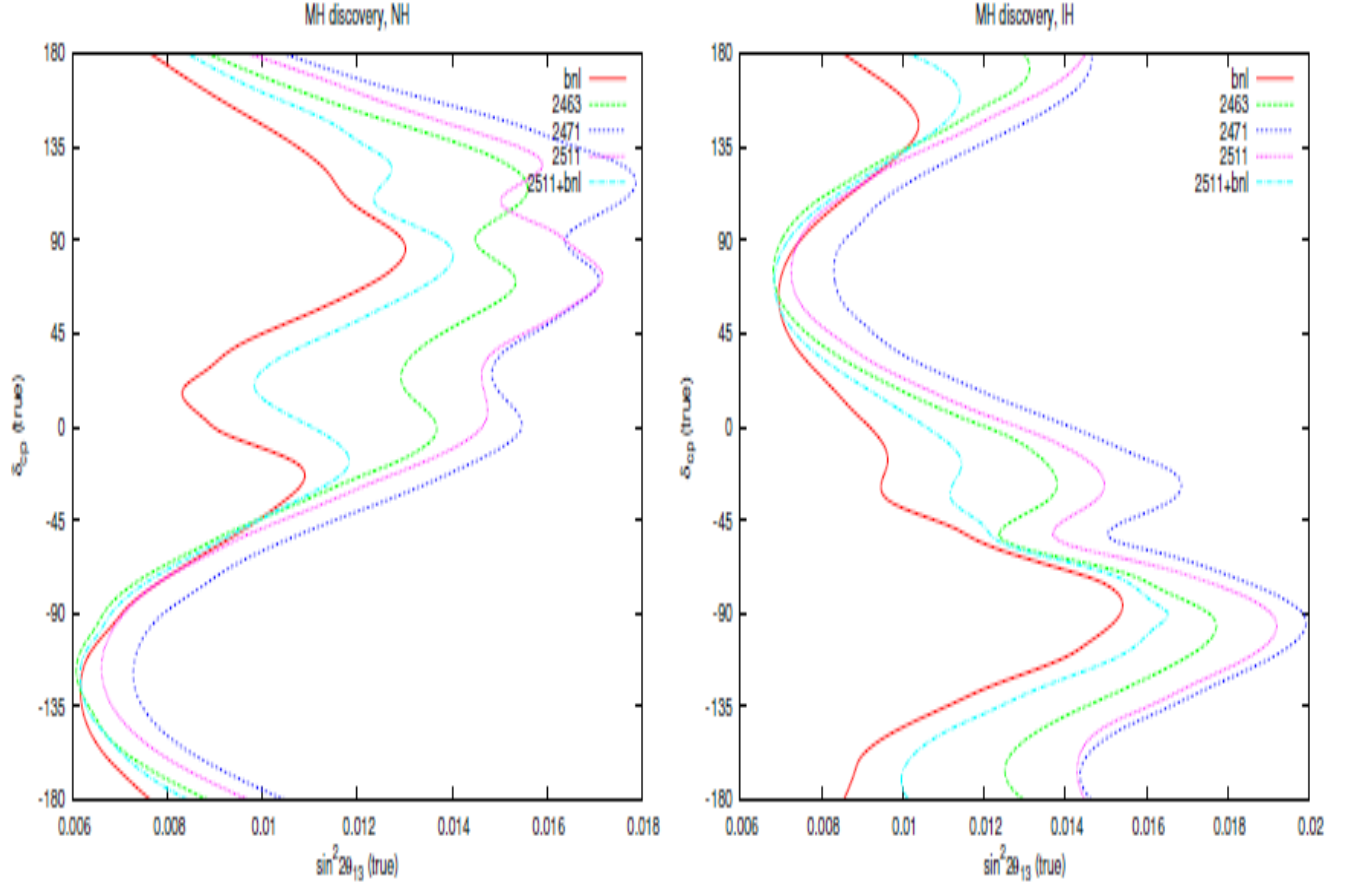


Figure 5: Physics sensitivities to the 3-1 mass hierarchy obtained from different candidate beams using a 200kT water Cerenkov detector at DUSEL with 5 yrs ν + 5yrs $\bar{\nu}$ running. The AGS 28 GeV beam at 700kW (red), the 2009 LBNE 120 GeV beam at 700kW (green dashed line), the LBNE Sep 2010 120 GeV CDR beam (blue dashed line), the Aug 2010 LBNE 120 GeV beam (magenta dashed line). (D. Mohapatra, LBNE-doc-2683).

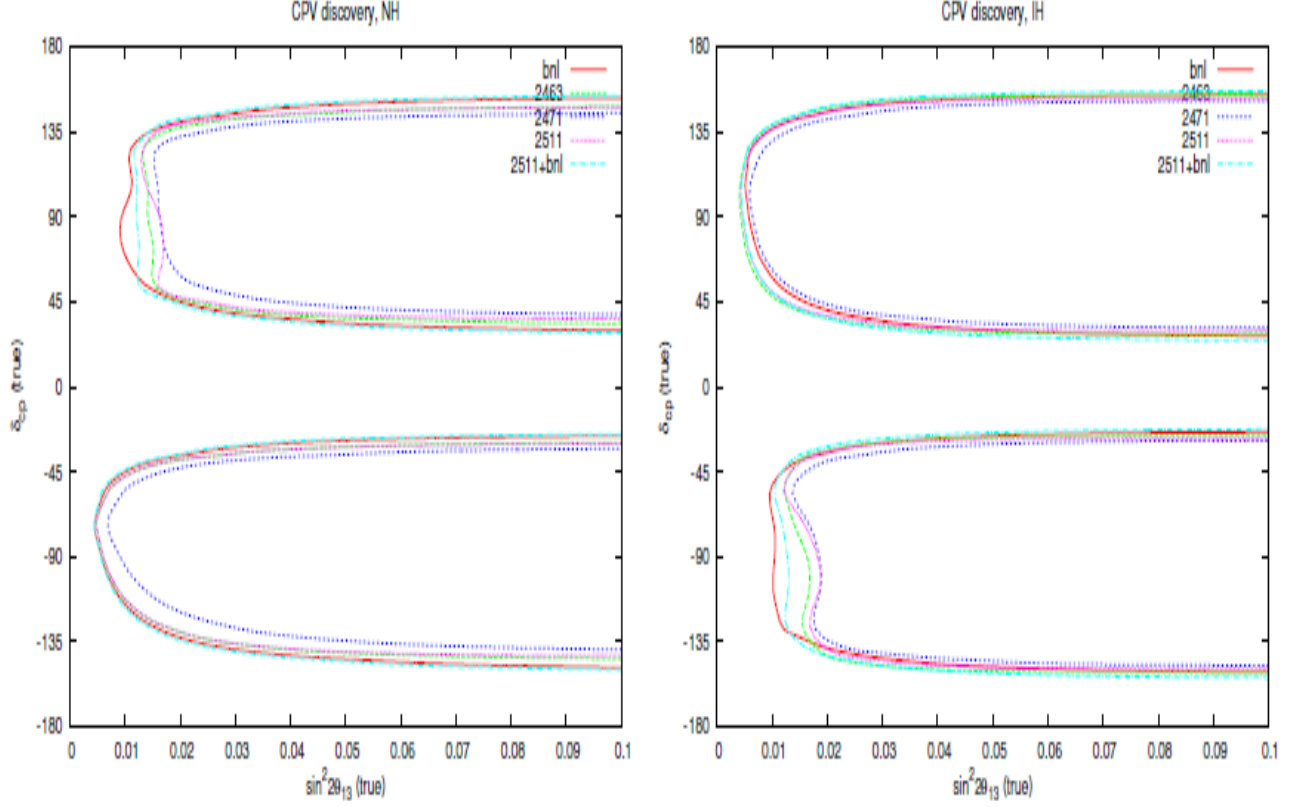


Figure 6: The physics sensitivities for CP violation obtained from different candidate beams using a 200kT water Cerenkov detector at DUSEL with 5 yrs ν + 5yrs $\bar{\nu}$ running. The AGS 28 GeV beam at 700kW (red), the 2009 LBNE 120 GeV beam at 700kW (green dashed line), the LBNE Sep 2010 120 GeV CDR beam (blue dashed line), the Aug 2010 LBNE 120 GeV beam (magenta dashed line). (D. Mohapatra, LBNE-doc-2683).

2 Optimization of Pion Production

The first step in understanding the impact of the proton beam energy on the performance of LBNE is a detailed study of the hadron production rate from the beam target. Since the majority of neutrinos in the LBNE energy range of interest come from pions, we will focus primarily on determining the maximal π^+ production rate as a function of proton beam energy and target material. Firstly, we need to determine the pion momentum range in which to maximize target production. The neutrino energy from a pion decay as a function of the decay angle θ and the pion boost γ is given by the following approximate formula:

$$E_\nu \sim 0.43E_\pi/(1 + \gamma^2\theta^2) \text{ for small } \theta \quad (1)$$

In Figure 7, the distribution of the pion momentum vs far detector neutrino energy obtained using the 2009 reference beam design is displayed. The first and 2nd oscillation maxima for $\delta_{cp} = 0$, $\Delta m_{31}^2 = 2.5 \times 10^{-3} \text{eV}^2$ are at $E_\nu = 2.4$ and 0.8 GeV respectively as indicated by the lines on the Figure. We find that the neutrino production is dominated by neutrinos at small angles where $E_\nu \sim 0.43E_\pi$.

Based on the approximation shown above and the oscillation probabilities shown in Figures 1 and 2 we have identified 5 pion momentum regions for optimization as shown in Table 2.

Table 2: Selection of pion energy ranges with sensitivity to particular LBNE LBL physics

E_π range	E_ν range	Physics
< 1 GeV	< 0.4 GeV	ν_e appearance from the solar term dominates
1-3 GeV	0.4-1.25 GeV	CP effects dominate
3-6 GeV	1.1-2.5 GeV	CP and mass hierarchy degenerate
6-10 GeV	2.1-4 GeV	mass hierarchy dominates
> 10 GeV	> 4 GeV	CC ν_τ appearance signal NC backgrounds for ν_e appearance

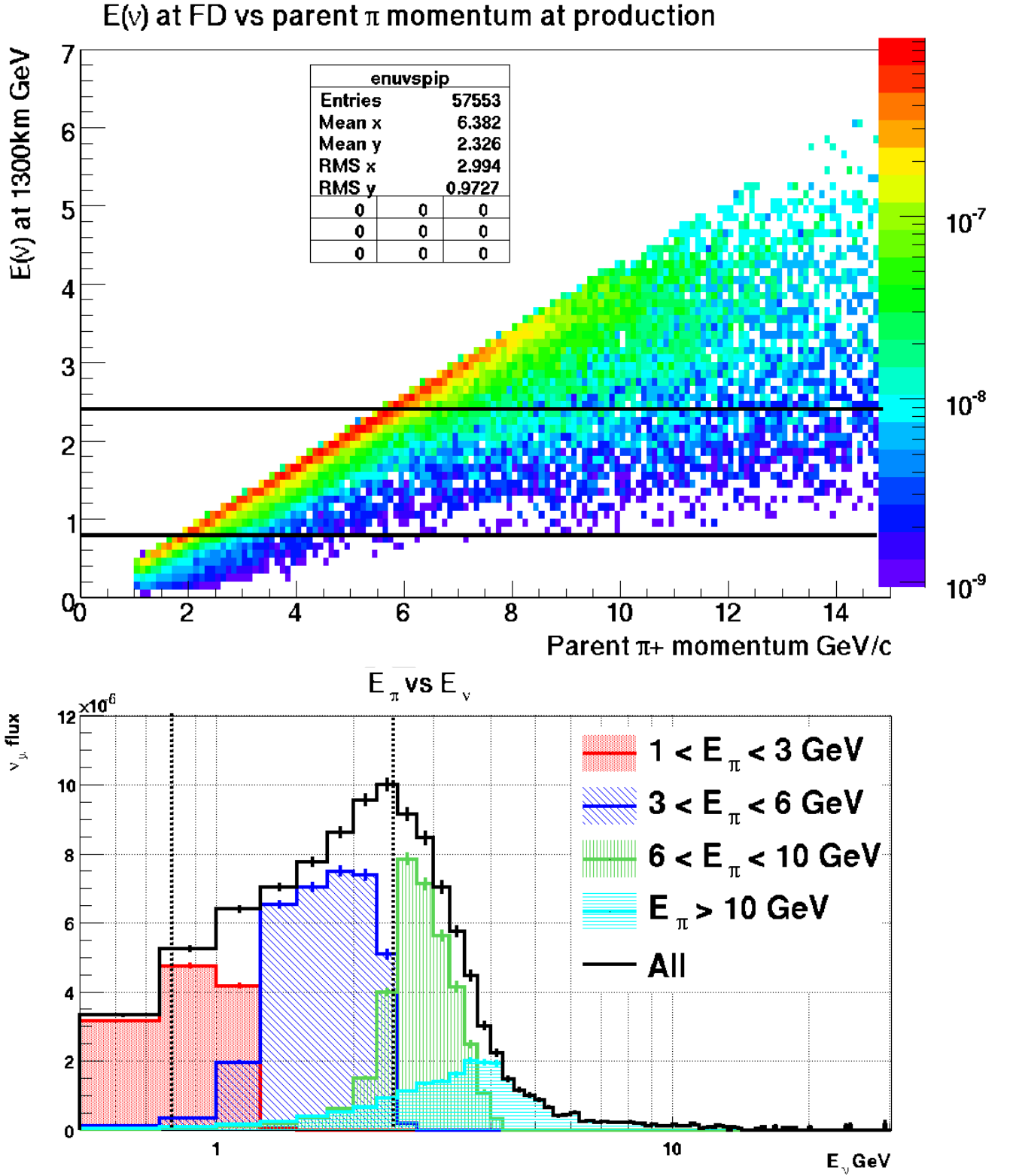


Figure 7: Neutrino energy at DUSEL vs π^+ production momentum. The lines at $E_\nu = 2.4$ and 0.8 GeV correspond to the first and second $\nu_\mu \rightarrow \nu_e$ oscillation maxima for normal hierarchy and $\delta_{cp} = 0$

2.1 Pion Production and Target Material

We simulated a wide range of potential target materials using FLUKA08 to study pion production. A proton beam with a momentum of 120 GeV with a Gaussian profile and $\sigma_x = \sigma_y = 0.15$ cm was initially used. Each target is a solid cylinder that is two interaction lengths long and has a radius of 0.45cm. Most targets were made out of pure materials. Three different types of Graphite with different densities were simulated. We also simulated a target composed of cubic Boron Nitride (c-BN) as an example of a high density, low-Z target. We realise c-BN is not a good candidate high power proton beam target material but we include it in our studies. We also included a target composed of Super-Invar, an alloy with the following composition: 62.66% Fe, 31.26% Ni, 5.36% Co, 0.39 % MN, 0.09% Si, 0.08% Cu, 0.07% Al, 0.05% C, 0.03% Cr, 0.01% S and a density of 8.15 g/cm³.

The total number of pions produced per proton from each target is shown in the bar chart in Figure 8. The materials are arranged from left to right in order of increasing Z.

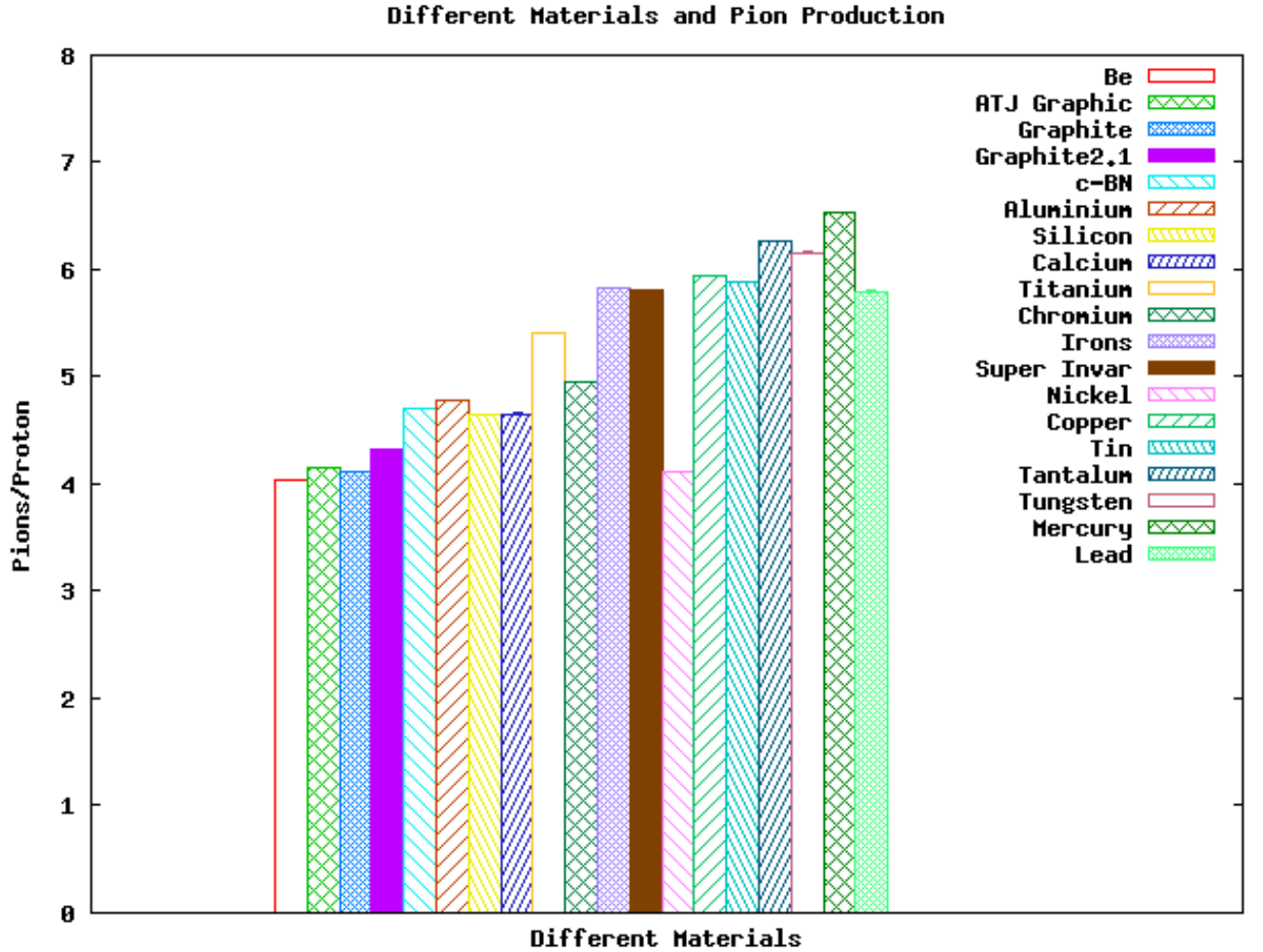


Figure 8: Total pion production from targets of different material. The proton beam energy is 120 GeV. Targets are cylindrical with a radius=0.45cm (3σ beam width) and length=2 nuclear interaction lengths. The materials are arranged from left to right as a function of increasing Z.

We observe that in general the overall trend is that higher Z materials produce more pions per 120 GeV proton. The trend is not universal with notable exceptions like Nickel. Mercury

targets produce the most pions per proton, followed by Tantalum and Tungsten. We obtain 6.5 pions/120 GeV proton from a Mercury target as compared to 4 pions/120 GeV proton from a Beryllium target.

2.2 Pion Production vs Proton Beam Energy

We examined pion production from five different target materials using proton beams with energies from 10 to 120 GeV protons. The pion production yields per proton per GeV of proton energy as a function of proton beam energy are shown in Figures 9 to 13. The results are shown for the 5 pion momentum regions identified in Table 2. The yields are shown for cylindrical targets made from the following materials:

1. Graphite (low-Z)
2. c-BN (high density low-Z)
3. Super Invar (mid-Z),
4. Tantalum (solid ,high-Z).
5. Mercury (liquid,high-Z).

Each target is cylindrical, 2 interaction lengths long and with a radius of 0.45cm. All the proton beams have a Gaussian profile with $\sigma = 0.15\text{cm}$. We observe the following:

- Different target materials have a different pion yield dependence on proton beam energy.
- For pions with momenta in the range 0 to 3 GeV, the general trend is that the pion yield per proton-GeV decreases with proton energy for $E_p \geq 20$ GeV. The production of pions with momentum < 3 GeV is significantly higher in high-Z materials compared to low-Z materials for proton beam energies > 20 GeV.
- For a proton beam of 10 GeV, low-Z materials like graphite have the highest rate of pion production in the 1-3 GeV range of pion momentum. The trend is reversed when the proton beam energy is ≥ 20 GeV, with the high-Z materials outperforming low-Z.
- For pions in the range 3-6 GeV, the largest yield is from low-Z materials coupled with a proton beam energy of 30 GeV. At proton beam energies > 60 GeV both low and high-Z materials have similar yield.
- Low-Z materials have the highest pion production yield for pions with momentum 6 – 10GeV for all proton beam energies considered. The production peaks at proton energies from 40 to 60 GeV and falls for proton energies > 60 GeV.
- **For pions in the range 0-10 GeV, the optimal pion production is at proton beam energies < 60 GeV for all the materials studied.**

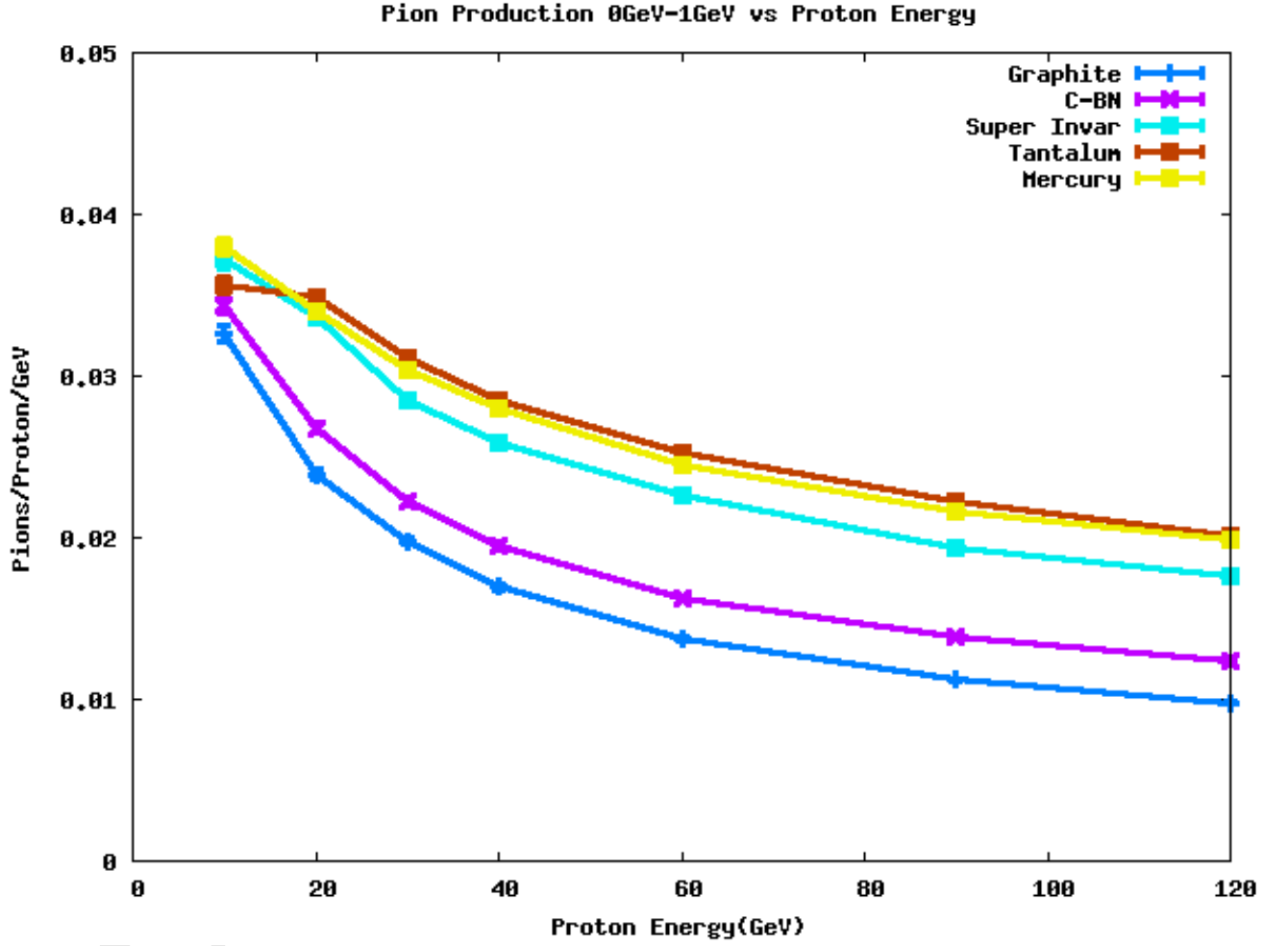


Figure 9: Pion production for pions with $E_\pi < 1$ GeV from targets of different material as a function of incident proton energy. Targets are cylindrical with a radius=0.45cm (3σ beam width) and length=2 nuclear interactions lengths.

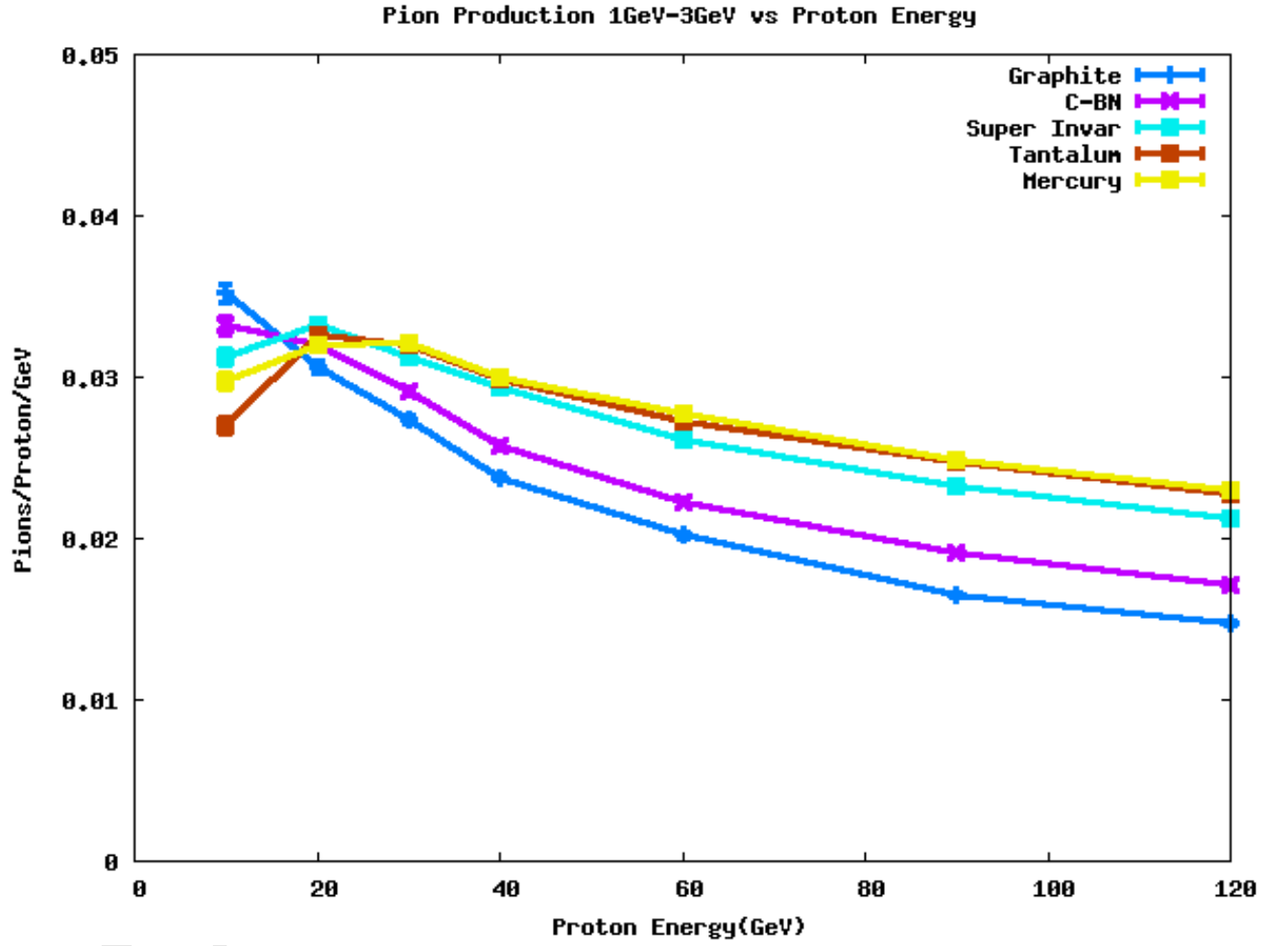


Figure 10: Pion production for pions with $1 < E_\pi < 3$ GeV from targets of different material as a function of incident proton energy. Targets are cylindrical with a radius=0.45cm (3σ beam width) and length=2 nuclear interactions lengths.

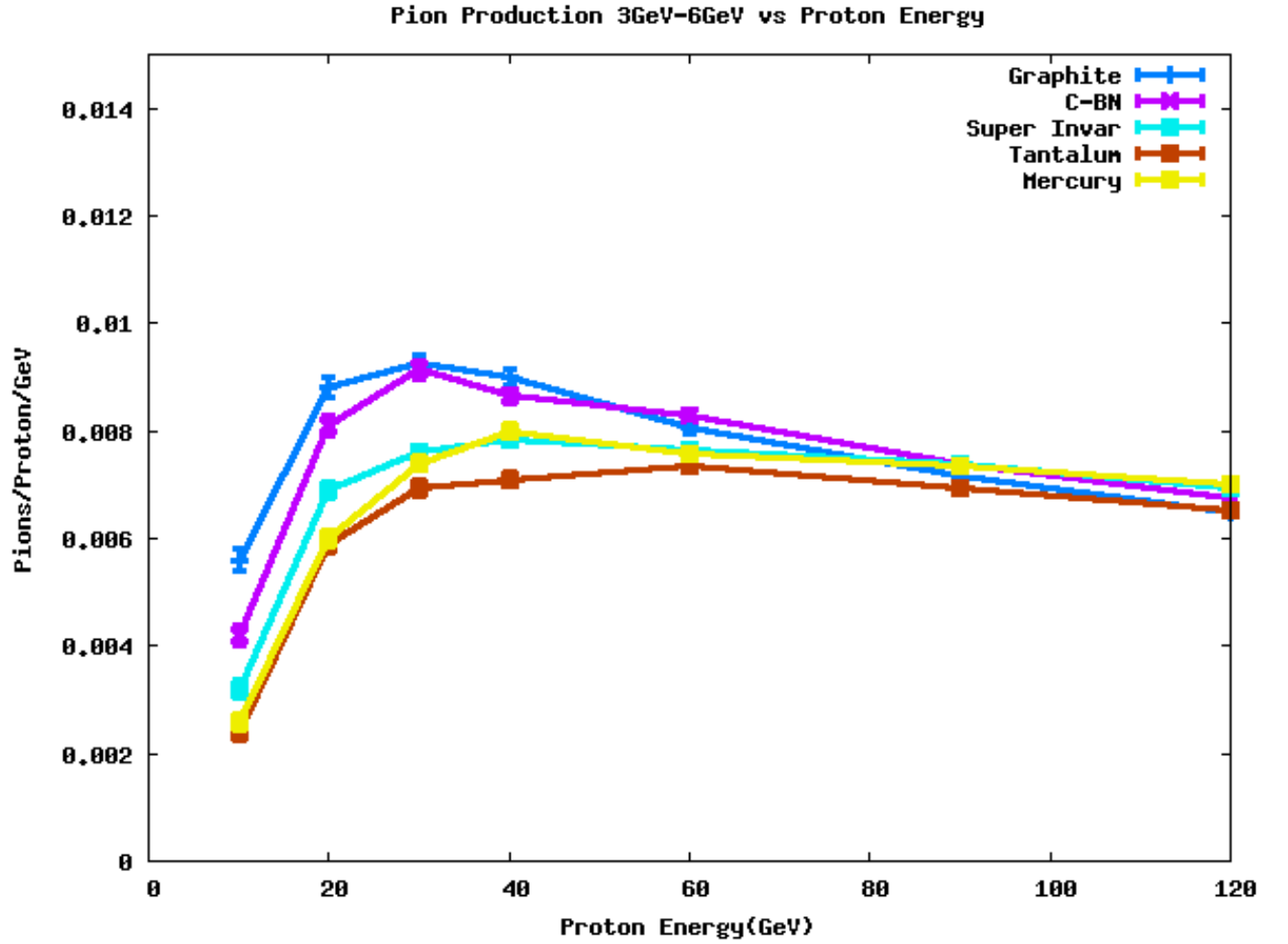


Figure 11: Pion production for pions with $3 < E_\pi < 6$ GeV from targets of different material as a function of incident proton energy. Targets are cylindrical with a radius=0.45cm (3σ beam width) and length=2 nuclear interactions lengths.

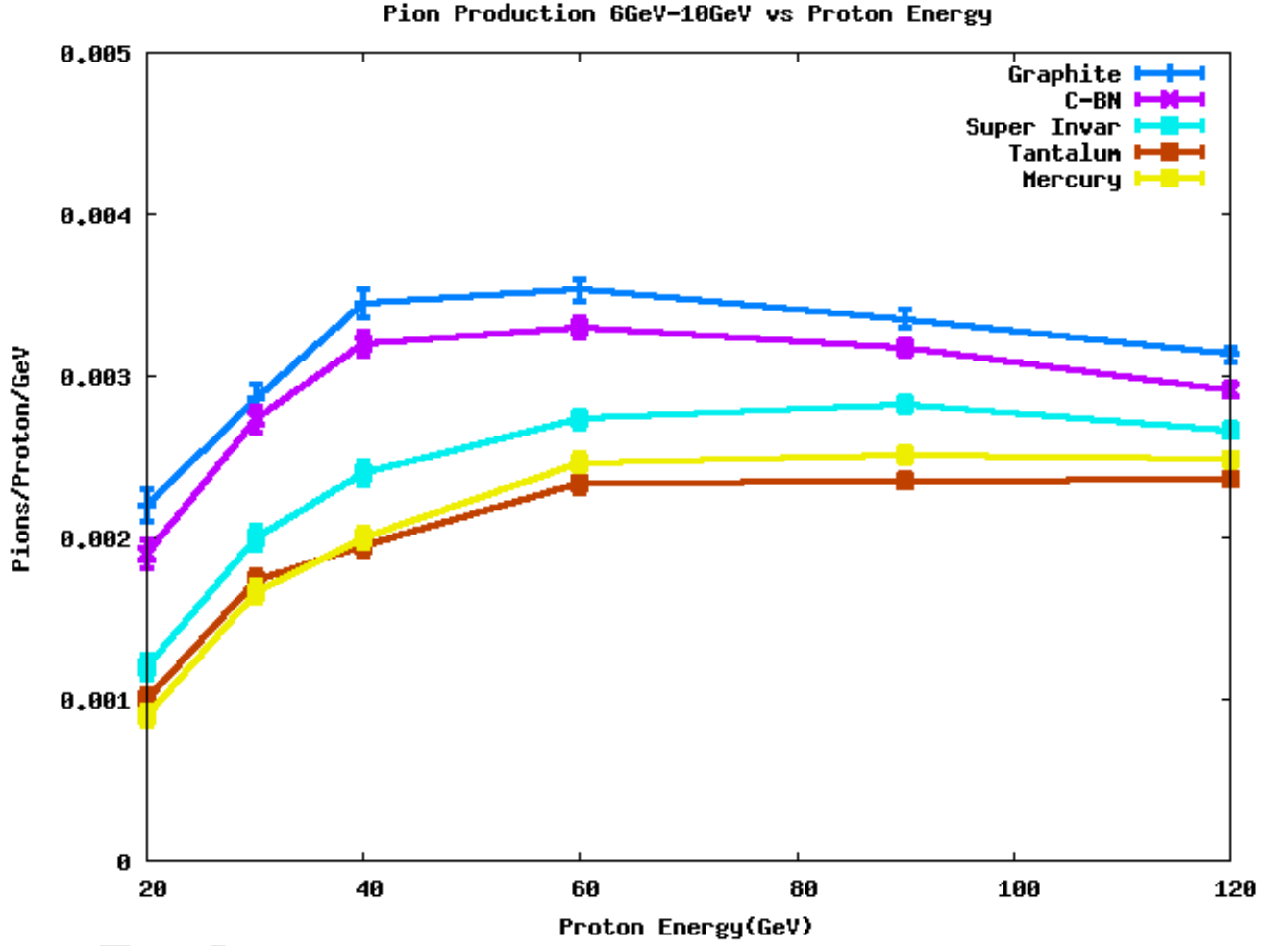


Figure 12: Pion production for pions with $6 < E_\pi < 10$ GeV from targets of different material as a function of incident proton energy. Targets are cylindrical with a radius=0.45cm (3σ beam width) and length=2 nuclear interactions lengths.

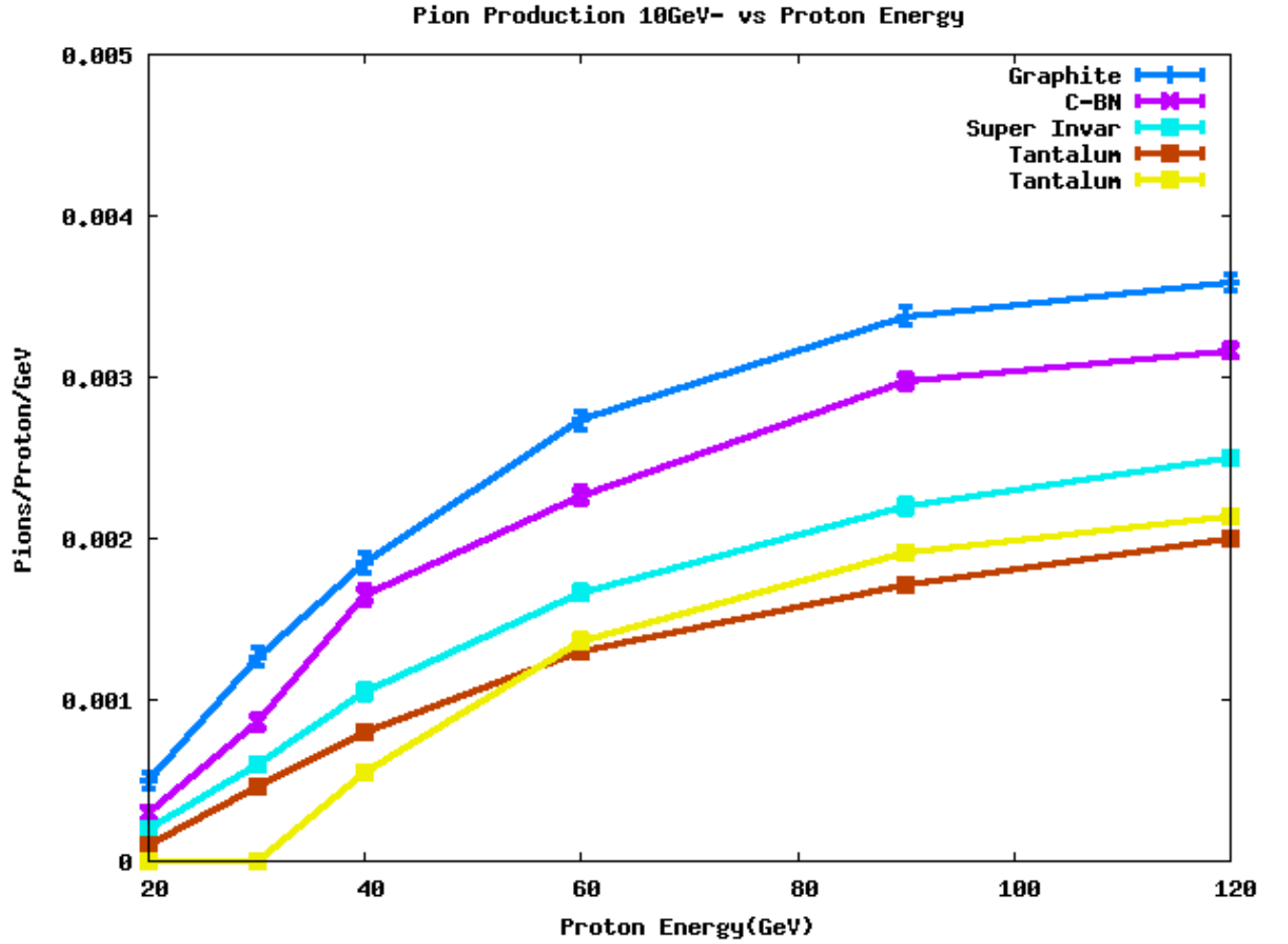


Figure 13: Pion production for pions with $E_\pi > 10$ GeV from targets of different material as a function of incident proton energy. Targets are cylindrical with a radius=0.45cm (3σ beam width) and length=2 nuclear interactions lengths.

2.3 Summary and Discussion

The pion production rate in different pion momentum ranges from various targets is summarized in Table 3. For the pion production from 0-10 GeV we present the target and proton beam energy that produces the *maximum* pions per proton-GeV. For the pion production > 10 GeV we present the target and proton beam energy that produces the *minimum* pions per proton-GeV. There are five combinations of target materials and proton energies summarized:

- Option I: This option represents the optimal combination of material and proton beam energy in each pion momentum range under consideration. This is the maximum pion production per proton-GeV obtained in each pion momentum range.
- Option II: The optimal choice of materials to maximize pion production for a proton beam of 40 GeV. This proton beam energy represents the energy at which we find the maximum pion per proton-GeV rate for pions in the range 3-10 GeV which are the main origin of neutrinos in the region of the first oscillation maxima.
- Option III: The production rates using a hybrid graphite-tantalum target with the optimal beam energy of 40 GeV. By combining a high-Z and low-Z material at 40 GeV we can recover most of the optimal performance of Option II using a single target operating at a fixed beam energy. The design of low-Z/high-Z hybrid targets will be discussed in an forthcoming document.
- Option IV: The production rates using a graphite target with the optimal beam energy of 40 GeV.
- Option V: A graphite target at proton beam energies at 120 GeV - the current LBNE choice.

As shown in Table 3, the current LBNE choice of a graphite target with a 120 GeV proton beam is the worst performing option in terms of useful pion production per proton-GeV. In addition, the 120 GeV beam has the most pion production > 10 GeV which is the main contributor to higher energy neutrinos that produce NC backgrounds to the ν_e appearance signal at low energy. **For a graphite target, the analysis of the pion production data indicates that a primary proton beam energy of around 40 GeV is the optimal choice for LBNE. Lowering the proton beam energy from 120 GeV to 10 GeV with a graphite target would raise the pion yield per proton-GeV in the range $1 < p_\pi < 3$ GeV by a factor of 2.4.**

To enhance the low energy pion production in the range 1-3 GeV (CP effects) at proton beam energies > 20 GeV, a higher-Z target would need to be used. Preliminary studies indicate that a hybrid Graphite-Tantalum or Invar-Tantalum target at 40 GeV would increase the yield of low energy pions, while preserving the pion yield in the 3-6 GeV region and significantly reducing the pion yield above 10 GeV. The designs of such a target will be discussed in an upcoming report.

Table 3: Optimal π^+ production rates in different pion momentum ranges as a function of target material and proton beam energy. All targets are 2 interaction lengths long with radius 0.45cm ($3\sigma_{beam}$). The π^+ production rate is given as number of pions per proton per GeV of proton energy.

Pion momentum	0-1 GeV maximum	1-3 GeV maximum	3-6 GeV maximum	6-10 GeV maximum	> 10 GeV minimum
I. Optimal combination of materials and beam energy					
Material	Mercury	Graphite	Graphite	Graphite	Tantalum
Proton beam energy	10 GeV	10 GeV	30 GeV	40-60 GeV	< 30 GeV
π^+ production rate	0.038	0.036	0.0093	0.0035	0
II. Fixed proton beam energy of 40 GeV					
Material	Hg/Tantalum	Hg/Tantalum/Invar	Graphite	Graphite	Tantalum
Proton beam energy	40 GeV	40 GeV	40 GeV	40 GeV	40 GeV
π^+ production rate	0.029	0.030	0.0090	0.0035	0.0005
III. Graphite-Tantalum target beam energy of 40 GeV					
Material	C-Ta	C-Ta	C-Ta	C-Ta	C-Ta
Proton beam energy	40 GeV	40 GeV	40 GeV	40 GeV	40 GeV
π^+ production rate	0.026	0.031	0.0090	0.0030	0.0014
IV. Graphite target beam energy of 40 GeV					
Material	Graphite	Graphite	Graphite	Graphite	Graphite
Proton beam energy	40 GeV	40 GeV	40 GeV	40 GeV	40 GeV
π^+ production rate	0.017	0.024	0.0090	0.0035	0.0018
V. Graphite target beam energy of 120 GeV					
Material	Graphite	Graphite	Graphite	Graphite	Graphite
Proton beam energy	120 GeV	120 GeV	120 GeV	120 GeV	120 GeV
π^+ production rate	0.010	0.015	0.0065	0.0031	0.0036

3 Neutrino Production

The FLUKA08 simulations of a graphite target of radius 0.6cm and 2 interaction lengths was used as input to a GEANT 3.21 simulation of the LBNE beamline (GNUMI). The geometry of the beamline simulated is described in LBNE-doc-2214 as the 2008/2009 design. The two NuMI horns are used as focusing elements operated at 250kA with a separation of 6m between them. The target is embedded in NuMI horn 1. The decay pipe is evacuated with a radius of 2m and a length of 280m. The hadron flux from several FLUKA08 graphite target simulations with variable proton beam energies were propagated through the GNUMI simulation of the 2008/2009 beamline. The neutrino fluxes thus produced with different proton beam energies propagated to Homestake are documented in LBNE-doc-2463. We chose the 2008/09 beamline design to study the dependence on proton beam energy as it has the best physics sensitivity of all 120 GeV LBNE beam designs considered so far as shown in Figures 4 to 6.

3.1 Neutrino Production and Primary Proton Beam Energy

The neutrino fluxes obtained from the 2008/2009 simulations of the LBNE beamline with primary proton energies from 30 to 120 GeV are shown in Figure 14. The neutrino flux shown in the top figure is the unoscillated ν_μ flux at the Homestake baseline of 1300km given per m^2 per GeV per MW.yr. The bottom figure shows the ratio of the fluxes per unit power to the flux at 120 GeV. We find that the flux per unit power at 1 GeV increases by 40% when the beam energy is changed from 120 GeV to 30 GeV. The flux at the 1st oscillation maximum (2.4 GeV) decreases by less than 20% when the beam energy is changed from 30 to 120 GeV. The high energy flux > 5 GeV for a 30 GeV beam is $< 20\%$ of the high energy flux at 120 GeV. The maximum flux at the 1st oscillation maximum is obtained at a beam energy of 60 GeV and is 10% higher than the neutrino flux at 120 GeV. **The neutrino flux variation as a function of energy is consistent with the pion production results and indicate that the optimal beam energies for LBNE are between 30 and 60 GeV.**

The ν_e appearance spectra at Homestake obtained with different primary proton beam energies is shown in Figure 15. The appearance probability was computed assuming normal hierarchy, $\sin^2 2\theta_{13} = 0.04$, $\delta_{cp} = 0$, and $\Delta m_{31}^2 = 2.5 \times 10^{-3} \text{ eV}^2$. The spectra shown are the product of the fluxes in Figure 14 and the appearance probability. No detector assumptions are included. The non-elastic NC spectrum from the fluxes in Figure 14 is shown as a function of visible energy in Figure 15. The conversion from true neutrino energy to visible energy was obtained from a NUANCE based simulation. The energy of particles produced in the NC interaction is summed up to estimate the visible energy. The particles are required to have energy above Cherenkov threshold (calculation from M. Diwan). From 15, we find that the NC rate at a visible energy of 1 GeV with a 30 GeV beam is 1/2 the rate with a 120 GeV while the ν_e appearance signal at 1 GeV is 30 % higher with a 30 GeV beam as compared to a 120 GeV beam. From these studies we find that the highest yield of $\nu_\mu \rightarrow \nu_e$ and the lowest NC background at 1 GeV is obtained with a beam energy of 30 GeV. We have not yet studied the performance with lower beam energies. The integrated rates of oscillated CC ν_μ , NC, CC beam ν_e , CC ν_e appearance, and CC ν_τ appearance for different proton beam energies are summarized in Table 4. The largest total rate of ν_e appearance was obtained for beam energies from 60 to 90 GeV.

To estimate how well each beam energy performs we used the NC, ν_μ -misID and ν_e CC signal efficiencies in a water Cerenkov detector obtained from the following study

“Further study of neutrino oscillation with two detectors in Kamioka and Korea.” F. Dufour et. al. Phys.Rev.D81:093001,2010. arXiv:1001.5165 (hep-ph)

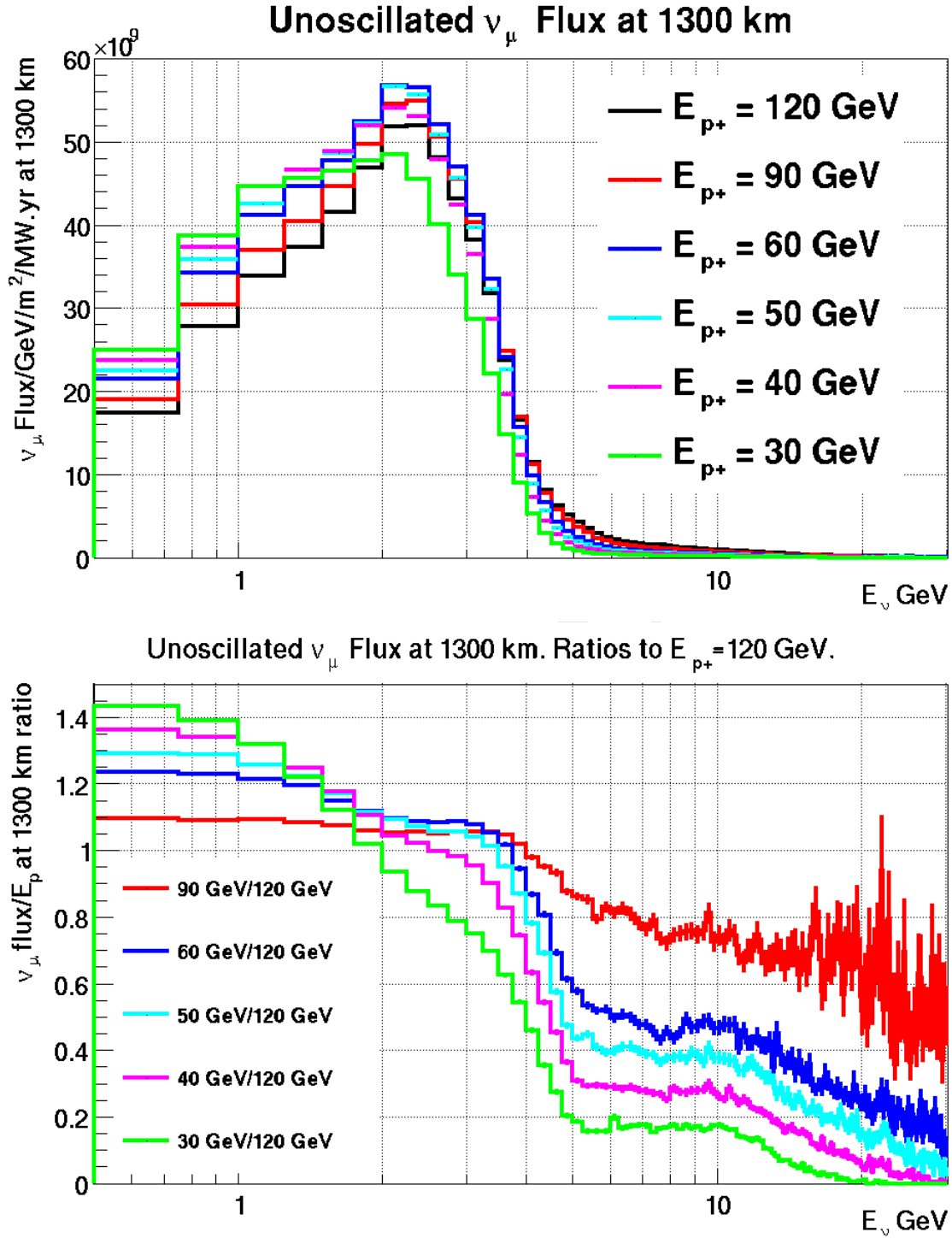


Figure 14: The ν_μ flux at DUSEL obtained with different proton beam energies. The target is a cylindrical graphite target with a radius of 0.6cm and 2 interaction lengths. The NuMI horns operated with 250kA are used for focusing with the target fully embedded in horn 1.

Appearance of ν_e with different E_{p+}

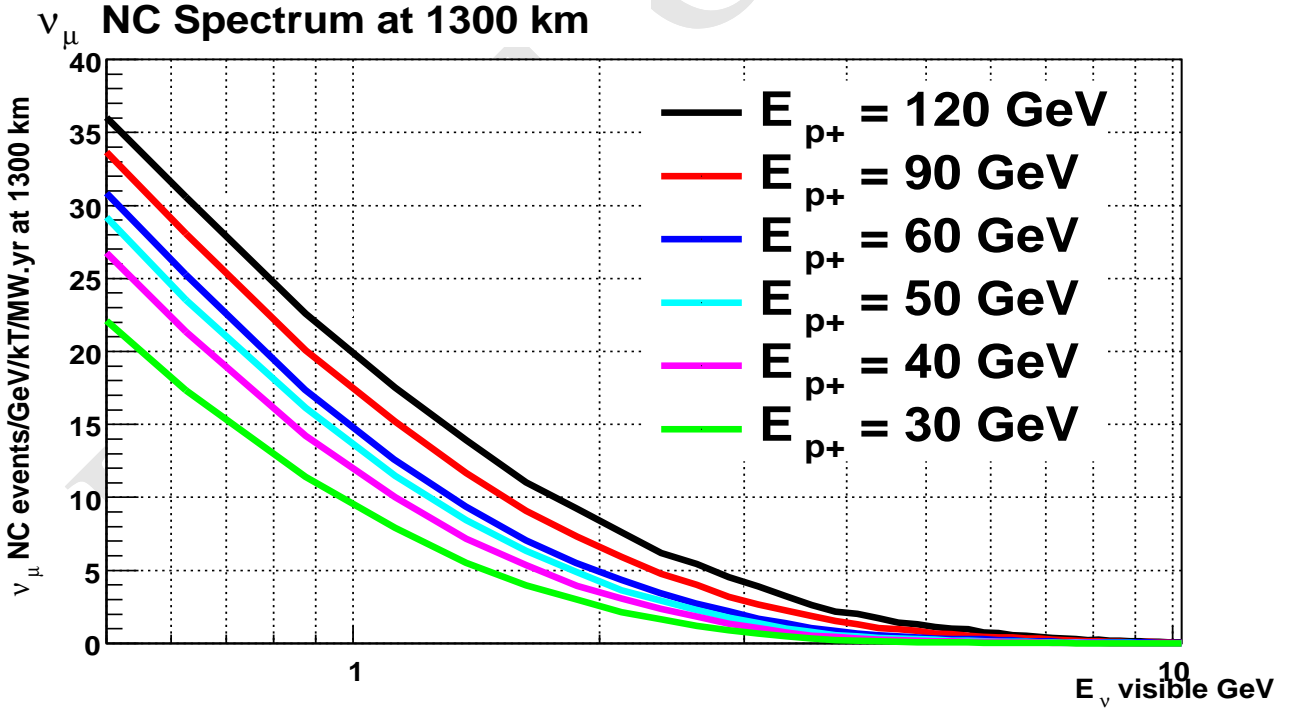
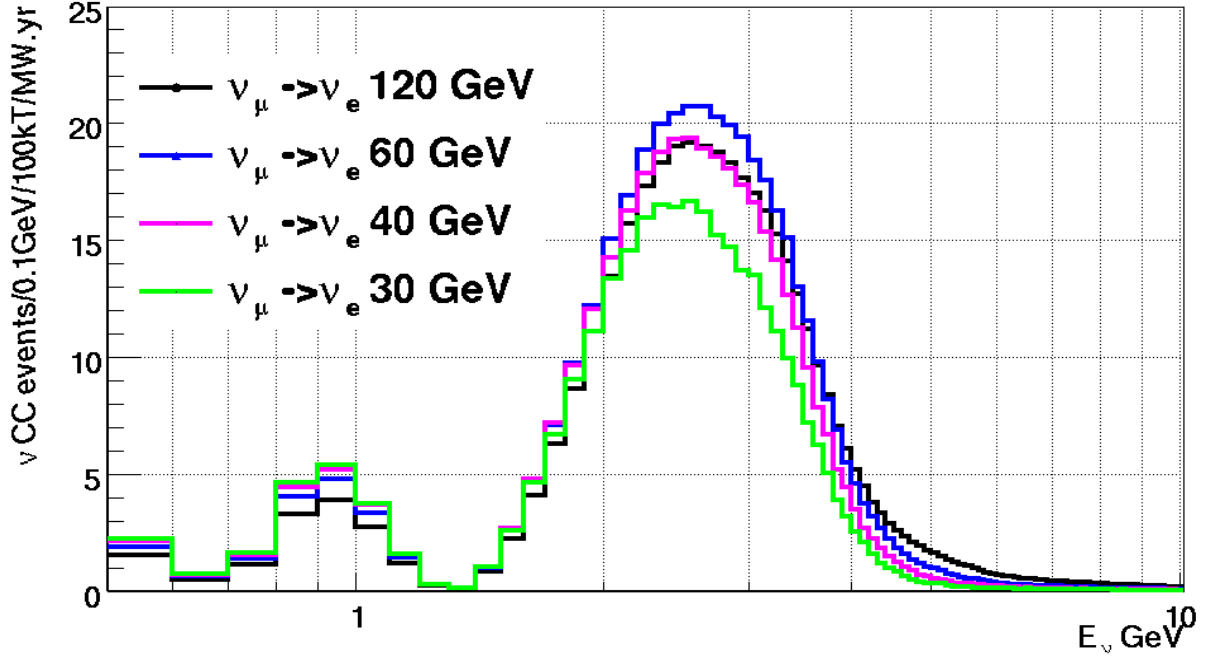


Figure 15: The ν_e appearance CC spectrum (top) and NC spectrum (bottom) at DUSEL obtained with different proton beam energies. For $\nu_\mu \rightarrow \nu_e$ oscillations a value of $\sin^2 2\theta_{13} = 0.04$ and $\Delta m_{31}^2 = 2.5 \times 10^{-3} \text{ eV}^2$ is used. No detector model is used.

Table 4: The total signal and background neutrino interaction rates at 1300 Km (Fermilab-HOMESTAKE) using different LBNE beam energies. The NC, beam ν_e and ν_e appearance signal rates are integrated over the energy range of 0.5 - 6 GeV. For NC, the visible energy obtained from the NUANCE event generator, is used. Rates are given per 100kT.MW.yr. For $\nu_\mu \rightarrow \nu_e$ oscillations a value of $\sin^2 2\theta_{13} = 0.04$ and $\Delta m_{31}^2 = 2.5 \times 10^{-3} \text{ eV}^2$ is used. F.O.M = $\epsilon_{\nu_e} S_{\nu_e} / \sqrt{\epsilon_{\nu_e} B_{\nu_e} + \epsilon_{NC} B_{NC} + \epsilon_{\nu_\mu} B_{\nu_\mu}}$. For WCD 1 $\epsilon_{\nu_e} = 0.15$, $\epsilon_{NC} = 0.008$, $\epsilon_{\nu_\mu} = 0.0005$ from the PWG. For WCD 2 $\epsilon_{\nu_e} = 0.4$, $\epsilon_{NC} = 0.04$, $\epsilon_{\nu_\mu} = 0.0014$ obtained from Table 5. For LAr $\epsilon_{\nu_e} = 0.8$, $\epsilon_{NC} = 0.01$, $\epsilon_{\nu_\mu} = 0.01$ from the Physics Working Group Report.

Beam Energy	ν_μ unosc CC	ν_μ osc CC (B_{ν_μ})	NC B_{NC}	ν_e beam CC B_{ν_e}	$\nu_\mu \rightarrow \nu_e$ CC S_{ν_e}	$\nu_\mu \rightarrow \nu_\tau$ CC S_{ν_τ}	F.O.M WCD 1	F.O.M WCD 2	F.O.M LAr
30 GeV	13K	3.7K (3.2K)	1.4K	100	303	15	8.58	12.09	21.59
40 GeV	16K	4.4K (3.5K)	1.8K	118	359	26	9.26	12.89	23.66
50 GeV	18K	4.9K (3.7K)	2.1K	120	387	36	9.59	13.22	24.95
60 GeV	18K	5.4K (3.8K)	2.3K	122	399	46	9.63	13.20	25.34
90 GeV	20K	6.7K (3.9K)	3.0K	120	399	77	9.03	12.12	24.85
120GeV	21K	7.7K (3.8K)	3.6K	117	384	103	8.29	10.97	23.59

The NC pre-selection efficiency for neutrinos with true energies from the range 0.85 to 10 GeV varies from 8 to 13 %. We used an average of 10% as the pre-cut efficiency for all NC events. Table 5 has the approximate overall selection efficiencies as a function of reconstructed energy obtained from (F. Dufour *et. al.*, 2010). We use a ν_e CC signal efficiency of $\epsilon_{\nu_e} = 0.4$, a NC acceptance efficiency of $\epsilon_{NC} = 0.04$ and ν_μ mis-ID efficiency of $\epsilon_{\nu_\mu} = 0.0014$. For each beam energy, we estimate a Figure-of-Merit, F.O.M = $\epsilon_{\nu_e} S_{\nu_e} / \sqrt{\epsilon_{\nu_e} B_{\nu_e} + \epsilon_{NC} B_{NC} + \epsilon_{\nu_\mu} B_{\nu_\mu}}$. The F.O.M thus calculated is shown in Table 4. The best F.O.M. is obtained at beam energies of 50-60 GeV.

Table 5: T2KK ν_e overall signal and background selection efficiencies from the SuperK simulation (F. Dufour et. al., 2010). For the ν_μ mis-ID background, we have assumed that the true neutrino energy and reconstructed energy range are the same. For the NC background, we assumed the pre-cut efficiency is 10% for all neutrinos.

Reconstructed energy	ν_e CC ϵ_{ν_e}	NC ϵ_{NC}	ν_μ mis-ID ϵ_{ν_μ}
0.35-0.85 GeV	70 %	2.5%	0.16 %
0.85-1.5 GeV	56 %	2.7%	0.09 %
1.5-2.0 GeV	46 %	3.0%	0.15 %
2.0-3.0 GeV	40 %	4.0%	0.14 %
3.0-4.0 GeV	36 %	5.0%	0.22 %
4.0-5.0 GeV	34 %	6.5%	0.55 %

4 Physics Sensitivity Studies

DRAFT COPY

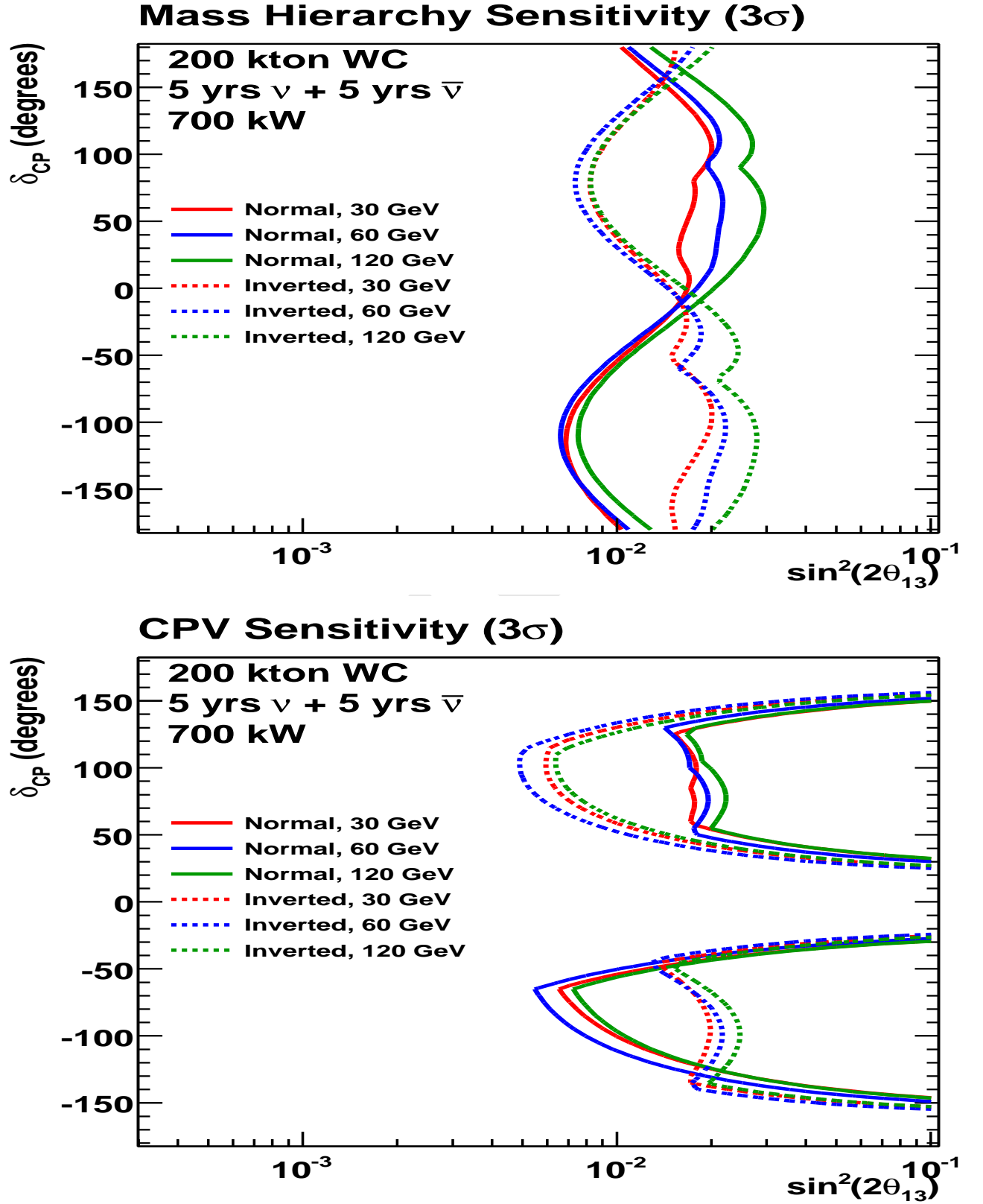


Figure 16: Sensitivity to the mass hierarchy (top) and CP violation (bottom) using 30,60 and 120 GeV beams with an exposure of 700kW 5+5 yrs and a 200kT WCD.

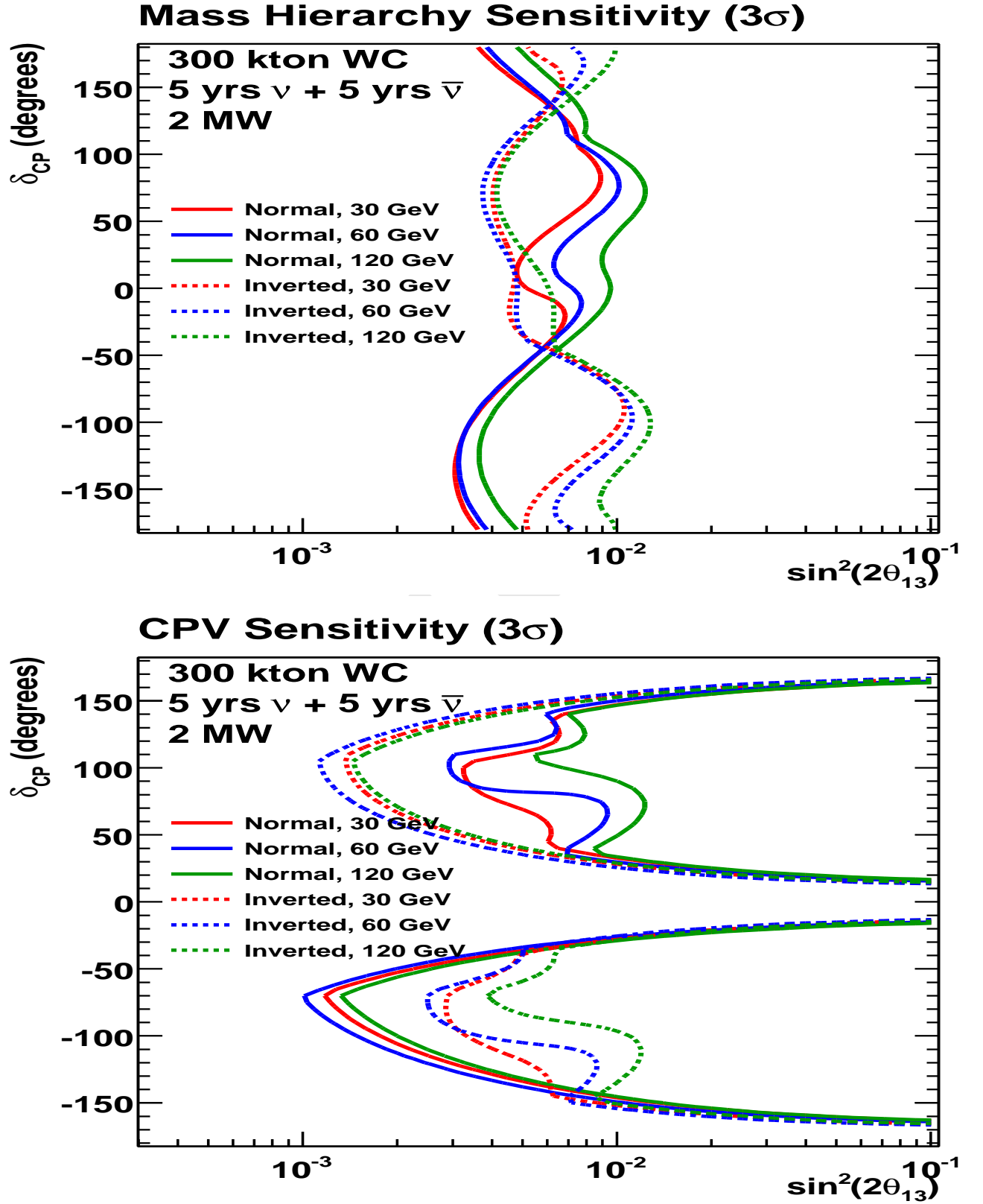


Figure 17: Sensitivity to the mass hierarchy (top) and CP violation (bottom) using 30,60 and 120 GeV beams with an exposure of 2MW 5+5 yrs and a 300kT WCD.

5 Summary and Conclusions

Recent LBNE sensitivity studies (D. Mohapatra, LBNE-doc-2683) have indicated that boosting the neutrino flux around 1 GeV can significantly improve the sensitivity to the mass hierarchy and CP violation. Reducing the primary proton beam energy is one of the most promising options for boosting pion production in the range 1-3 GeV which produces neutrinos in the range 0.4-1.2 GeV. We studied the pion production efficiency from various target materials as a function of primary proton beam energy using FLUKA08. The maximum pion production per proton-GeV for pions with momentum from 1 to 3 GeV was obtained from a graphite target with an incident proton beam energy of 10 GeV. The maximum pion production in the range of 3 to 10 GeV - which produces neutrinos at the 1st oscillation maxima was obtained from a graphite target with a 40 GeV proton beam. To boost the production of pions in the 1-3 GeV region with incident proton beam energies > 20 GeV requires the use of high-Z or hybrid low-Z/high-Z targets. **For pions in the range 0-10 GeV, the optimal pion production is at proton beam energies of < 60 GeV for all the materials studied.** A preliminary analysis of the $\nu_\mu \rightarrow \nu_e$ appearance signal and backgrounds at Homestake using a graphite target and the NuMI focusing system indicates that the best signal yield and signal to background is obtained with a primary proton beam energy of 50-60 GeV.

List of Tables

1	Conventional neutrino 2-horn beam designs used in the sensitivity studies of LBNE-doc-2683. The BNL-AGS far detector neutrino flux used in this study was produced using the flux at the near detector scaled by $1/L^2$. The FNAL-MI fluxes are all from a FLUKA08/GEANT 3.21 simulation and are extrapolated properly to the far detector. All simulations use a cylindrical graphite target of 2 interaction lengths long with radius = 0.6 to 0.75 cm either partially (Aug 2010 flux) or wholly inserted in the the first horn.	7
2	Selection of pion energy ranges with sensitivity to particular LBNE LBL physics	11
3	Optimal π^+ production rates in different pion momentum ranges as a function of target material and proton beam energy. All targets are 2 interaction lengths long with radius 0.45cm ($3\sigma_{beam}$). The π^+ production rate is given as number of pions per proton per GeV of proton energy.	21
4	The total signal and background neutrino interaction rates at 1300 Km (Fermilab-HOMESTAKE) using different LBNE beam energies. The NC, beam ν_e and ν_e appearance signal rates are integrated over the energy range of 0.5 - 6 GeV. For NC, the visible energy obtained from the NUANCE event generator, is used. Rates are given per 100kT.MW.yr. For $\nu_\mu \rightarrow \nu_e$ oscillations a value of $\sin^2 2\theta_{13} = 0.04$ and $\Delta m_{31}^2 = 2.5 \times 10^{-3} \text{ eV}^2$ is used. F.O.M = $\epsilon_{\nu_e} S_{\nu_e} / \sqrt{\epsilon_{\nu_e} B_{\nu_e} + \epsilon_{NC} B_{NC} + \epsilon_{\nu_\mu} B_{\nu_\mu}}$. For WCD 1 $\epsilon_{\nu_e} = 0.15$, $\epsilon_{NC} = 0.008$, $\epsilon_{\nu_\mu} = 0.0005$ from the PWG. For WCD 2 $\epsilon_{\nu_e} = 0.4$, $\epsilon_{NC} = 0.04$, $\epsilon_{\nu_\mu} = 0.0014$ obtained from Table 5. For LAr $\epsilon_{\nu_e} = 0.8$, $\epsilon_{NC} = 0.01$, $\epsilon_{\nu_\mu} = 0.01$ from the Physics Working Group Report.	25
5	T2KK ν_e overall signal and background selection efficiencies from the SuperK simulation (F. Dufour et. al., 2010). For the ν_μ mis-ID background, we have assumed that the true neutrino energy and reconstructed energy range are the same. For the NC background, we assumed the pre-cut efficiency is 10% for all neutrinos.	26

List of Figures

1	The $\nu_\mu \rightarrow \nu_e$ oscillation probability for the LBNE to DUSEL baseline of 1300 km for different mixing parameter with normal hierarchy is shown as colored curves. The unoscillated CC ν_μ spectrum from an LBNE candidate beam is shown as the solid black histogram.	4
2	The $\nu_\mu \rightarrow \nu_e$ oscillation probability for the LBNE to DUSEL baseline of 1300 km for different mixing parameter with inverted hierarchy is shown as colored curves. The unoscillated CC ν_μ spectrum from an LBNE candidate beam is shown as the solid black histogram.	5
3	The ν_μ and $\bar{\nu}_\mu$ fluxes at DUSEL from different candidate beams. The AGS 28 GeV beam (red), the 2009 LBNE 120 GeV beam, the LBNE CDR beam (blue dashed line), the Aug 2010 LBNE 120 GeV beam (magenta dashed line). (D. Mohapatra, LBNE-doc-2683)	6

4	Physics sensitivities to non-zero θ_{13} obtained from different candidate beams using a 200kT water Cerenkov detector at DUSEL with 5 yrs ν + 5yrs $\bar{\nu}$ running. The AGS 28 GeV beam at 700kW (red), the 2009 LBNE 120 GeV beam at 700kW (green dashed line) , the LBNE Sep 2010 120 GeV CDR beam (blue dashed line), the Aug 2010 LBNE 120 GeV beam (magenta dashed line). (D. Mohapatra, LBNE-doc-2683).	8
5	Physics sensitivities to the 3-1 mass hierarchy obtained from different candidate beams using a 200kT water Cerenkov detector at DUSEL with 5 yrs ν + 5yrs $\bar{\nu}$ running. The AGS 28 GeV beam at 700kW (red), the 2009 LBNE 120 GeV beam at 700kW (green dashed line) , the LBNE Sep 2010 120 GeV CDR beam (blue dashed line), the Aug 2010 LBNE 120 GeV beam (magenta dashed line). (D. Mohapatra, LBNE-doc-2683).	9
6	The physics sensitivities for CP violation obtained from different candidate beams using a 200kT water Cerenkov detector at DUSEL with 5 yrs ν + 5yrs $\bar{\nu}$ running. The AGS 28 GeV beam at 700kW (red), the 2009 LBNE 120 GeV beam at 700kW (green dashed line) , the LBNE Sep 2010 120 GeV CDR beam (blue dashed line), the Aug 2010 LBNE 120 GeV beam (magenta dashed line). (D. Mohapatra, LBNE-doc-2683).	10
7	Neutrino energy at DUSEL vs π^+ production momentum. The lines at $E_\nu = 2.4$ and 0.8 GeV correspond to the first and second $\nu_\mu \rightarrow \nu_e$ oscillation maxima for normal hierarchy and $\delta_{cp} = 0$	12
8	Total pion production from targets of different material. The proton beam energy is 120 GeV. Targets are cylindrical with a radius=0.45cm (3σ beam width) and length=2 nuclear interaction lengths. The materials are arranged from left to right as a function of increasing Z.	13
9	Pion production for pions with $E_\pi < 1$ GeV from targets of different material as a function of incident proton energy. Targets are cylindrical with a radius=0.45cm (3σ beam width) and length=2 nuclear interactions lengths. . .	15
10	Pion production for pions with $1 < E_\pi < 3$ GeV from targets of different material as a function of incident proton energy. Targets are cylindrical with a radius=0.45cm (3σ beam width) and length=2 nuclear interactions lengths. . .	16
11	Pion production for pions with $3 < E_\pi < 6$ GeV from targets of different material as a function of incident proton energy. Targets are cylindrical with a radius=0.45cm (3σ beam width) and length=2 nuclear interactions lengths. . .	17
12	Pion production for pions with $6 < E_\pi < 10$ GeV from targets of different material as a function of incident proton energy. Targets are cylindrical with a radius=0.45cm (3σ beam width) and length=2 nuclear interactions lengths. . .	18
13	Pion production for pions with $E_\pi > 10$ GeV from targets of different material as a function of incident proton energy. Targets are cylindrical with a radius=0.45cm (3σ beam width) and length=2 nuclear interactions lengths. . .	19
14	The ν_μ flux at DUSEL obtained with different proton beam energies. The target is a cylindrical graphite target with a radius of 0.6cm and 2 interaction lengths. The NuMI horns operated with 250kA are used for focusing with the target fully embedded in horn 1.	23
15	The ν_e appearance CC spectrum (top) and NC spectrum (bottom) at DUSEL obtained with different proton beam energies. For $\nu_\mu \rightarrow \nu_e$ oscillations a value of $\sin^2 2\theta_{13} = 0.04$ and $\Delta m_{31}^2 = 2.5 \times 10^{-3} \text{ eV}^2$ is used. No detector model is used.	24
16	Sensitivity to the mass hierarchy (top) and CP violation (bottom) using 30,60 and 120 GeV beams with an exposure of 700kW 5+5 yrs and a 200kT WCD. .	28

17	Sensitivity to the mass hierarchy (top) and CP violation (bottom) using 30,60 and 120 GeV beams with an exposure of 2MW 5+5 yrs and a 300kT WCD. . .	29
18	Energy deposition (GeV/proton/cm ³) by a 30 GeV Gaussian proton beam with $\sigma = 0.15\text{cm}$ in a cylindrical graphite target ($r=0.45\text{cm}$, $L=96\text{cm}$, $\rho = 1.76\text{ g/cm}^3$). The proton beam is incident from the left. The integrated energy deposition in the graphite target is 0.785 GeV/proton. The maximum energy density in the center of the target (integrated from $z = 0$ to 10cm) is 0.085 GeV/cm ³ /proton.	36
19	Energy deposition (GeV/proton/cm ³) by a 60 GeV Gaussian proton beam with $\sigma = 0.15\text{cm}$ in a cylindrical graphite target ($r=0.45\text{cm}$, $L=96\text{cm}$, $\rho = 1.76\text{ g/cm}^3$). The proton beam is incident from the left. The integrated energy deposition in the graphite target is 1.04 GeV/proton. The maximum energy density in the center of the target (integrated from $z = 0$ to 10cm) is 0.102 GeV/cm ³ /proton.	37
20	Energy deposition (GeV/proton/cm ³) by a 120 GeV Gaussian proton beam with $\sigma = 0.15\text{cm}$ in a cylindrical graphite target ($r=0.45\text{cm}$, $L=96\text{cm}$, $\rho = 1.76\text{ g/cm}^3$). The proton beam is incident from the left. The integrated energy deposition in the graphite target is 1.49 GeV/proton. The maximum energy density in the center of the target (integrated from $z = 0$ to 10cm) is 0.110 GeV/cm ³ /proton.	38
21	Integrated energy deposition (GeV/proton/ E_p) in cylindrical targets vs primary proton beam energy for different materials.	39
22	Simplified LBNE target and decay pipe shielding geometry simulated in FLUKA08. A graphite target of radius 0.6cm and 2 interaction lengths is located at 0,0,0. The proton beam is incident from the left	40
23	Energy deposition in the concrete shielding of a cylindrical 2m radius 250m long decay pipe. A proton beam of 30 GeV is incident from the left on a graphite target of 2 interaction lengths located at $z=0\text{m}$. The decay pipe is filled with He at 1atm. There are no focusing elements included in this simulation. The energy density is given in units of Joules/16e13 protons/cm ³	41
24	Energy deposition in the concrete shielding of a cylindrical 2m radius 250m long decay pipe. A proton beam of 60 GeV is incident from the left on a graphite target of 2 interaction lengths located at $z=0\text{m}$. The decay pipe is filled with He at 1atm. There are no focusing elements included in this simulation. The energy density is given in units of Joules/8e13 protons/cm ³	42
25	Energy deposition in the concrete shielding of a cylindrical 2m radius 250m long decay pipe. A proton beam of 120 GeV is incident from the left on a graphite target of 2 interaction lengths located at $z=0\text{m}$. The decay pipe is filled with He at 1atm. There are no focusing elements included in this simulation. The energy density is given in units of Joules/4e13 protons/cm ³	43
26	Star (inelastic interaction) density in the concrete shielding of a cylindrical 2m radius 250m long decay pipe. A proton beam of 30 GeV is incident from the left on a graphite target of 2 interaction lengths located at $z=0\text{m}$. The decay pipe is filled with He at 1atm. There are no focusing elements included in this simulation. The star density is given in units of Stars/16e13 protons/cm ³	44
27	Star (inelastic interaction) density in the concrete shielding of a cylindrical 2m radius 250m long decay pipe. A proton beam of 60 GeV is incident from the left on a graphite target of 2 interaction lengths located at $z=0\text{m}$. The decay pipe is filled with He at 1atm. There are no focusing elements included in this simulation. The star density is given in units of Stars/8e13 protons/cm ³	45

28	Star (inelastic interaction) density in the concrete shielding of a cylindrical 2m radius 250m long decay pipe. A proton beam of 120 GeV is incident from the left on a graphite target of 2 interaction lengths located at $z=0$ m. The decay pipe is filled with He at 1atm. There are no focusing elements included in this simulation. The star density is given in units of Stars/ $4e13$ protons/ cm^3	46
29	FNAL MI Beam power as a function of primary proton beam energy for various upgrade options. (Bob Zwaska)	47
30	Neutrino flux from the BNL-AGS beam design as compared to the NuMI based MI designs at 30 and 120 GeV. All simulations used the FLUKA05-08/GEANT 3.21 based GNUMI framework and the flux is correctly extrapolated to the far detector. The target simulated is identical in both designs: high density graphite $r=0.6$ cm and 2 interaction lengths.	48

DRAFT COPY

A Energy Deposition

A.1 Target

DRAFT COPY

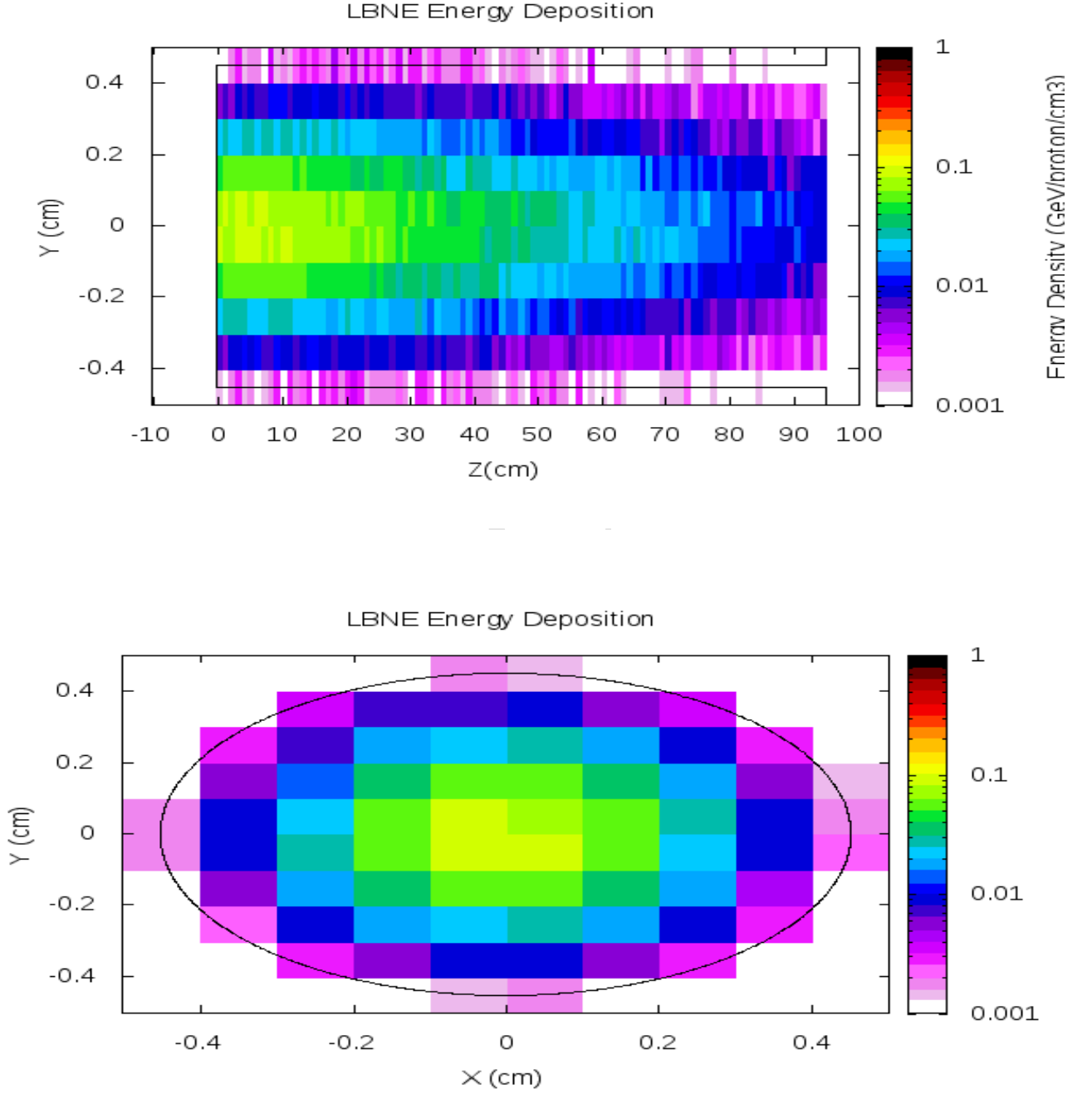


Figure 18: Energy deposition (GeV/proton/cm^3) by a 30 GeV Gaussian proton beam with $\sigma = 0.15\text{cm}$ in a cylindrical graphite target ($r=0.45\text{cm}$, $L=96\text{cm}$, $\rho = 1.76 \text{ g/cm}^3$). The proton beam is incident from the left. The integrated energy deposition in the graphite target is 0.785 GeV/proton . The maximum energy density in the center of the target (integrated from $z = 0$ to 10cm) is $0.085 \text{ GeV/cm}^3/\text{proton}$.

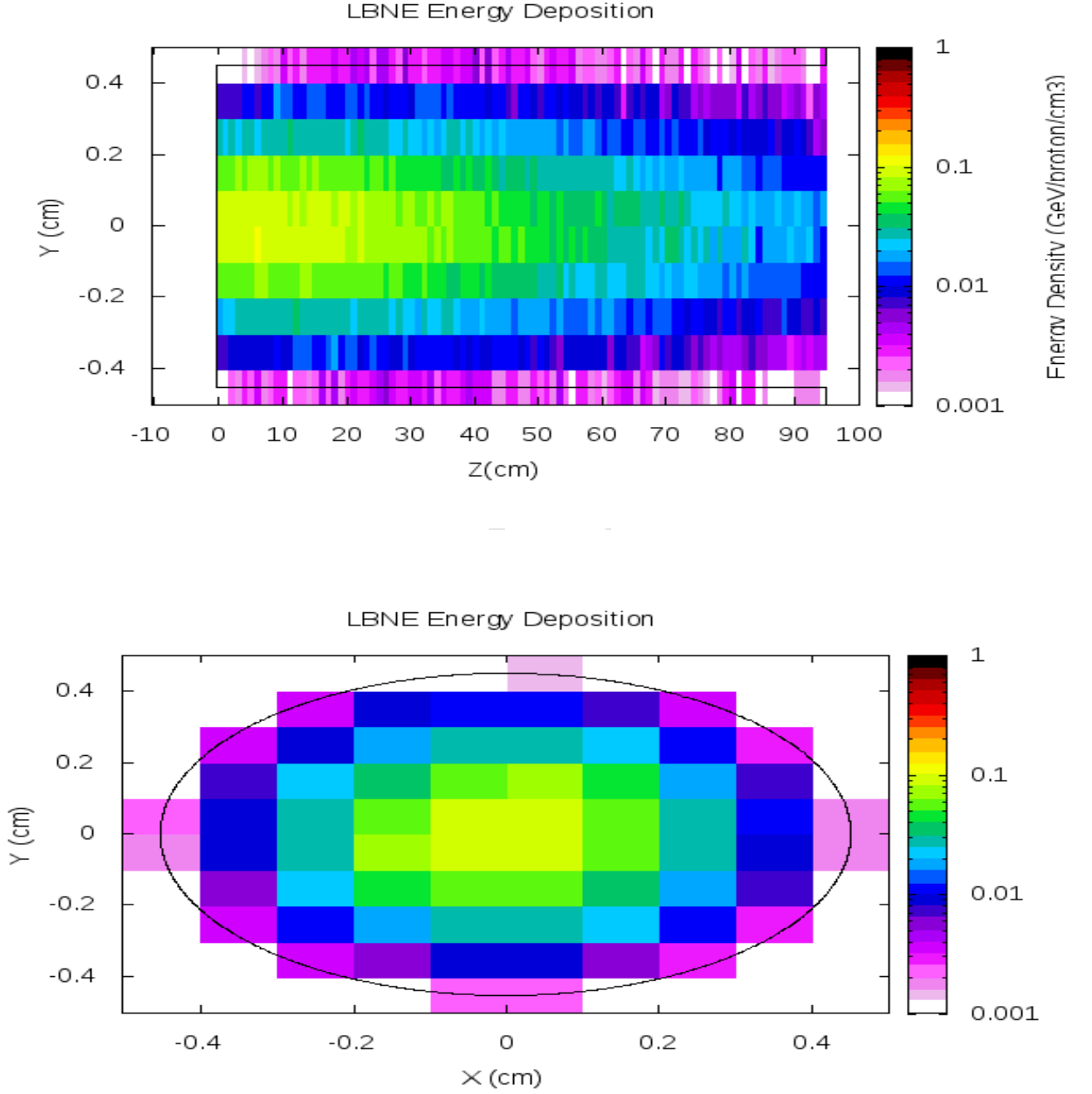


Figure 19: Energy deposition (GeV/proton/cm^3) by a 60 GeV Gaussian proton beam with $\sigma = 0.15\text{cm}$ in a cylindrical graphite target ($r=0.45\text{cm}$, $L=96\text{cm}$, $\rho = 1.76 \text{ g/cm}^3$). The proton beam is incident from the left. The integrated energy deposition in the graphite target is 1.04 GeV/proton . The maximum energy density in the center of the target (integrated from $z = 0$ to 10cm) is $0.102 \text{ GeV/cm}^3/\text{proton}$.

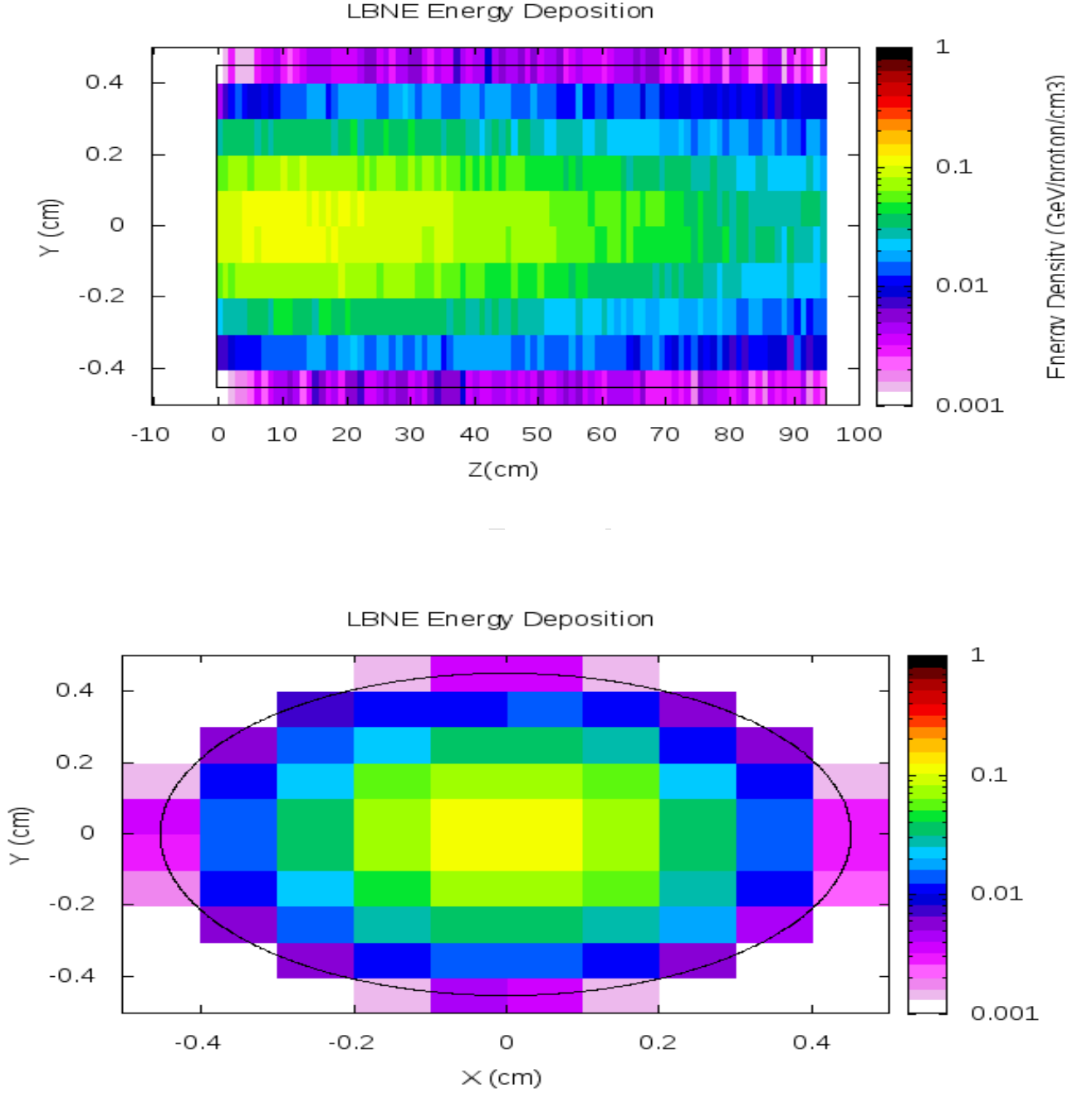


Figure 20: Energy deposition (GeV/proton/cm^3) by a 120 GeV Gaussian proton beam with $\sigma = 0.15\text{cm}$ in a cylindrical graphite target ($r=0.45\text{cm}$, $L=96\text{cm}$, $\rho = 1.76 \text{ g/cm}^3$). The proton beam is incident from the left. The integrated energy deposition in the graphite target is 1.49 GeV/proton . The maximum energy density in the center of the target (integrated from $z = 0$ to 10cm) is $0.110 \text{ GeV/cm}^3/\text{proton}$.

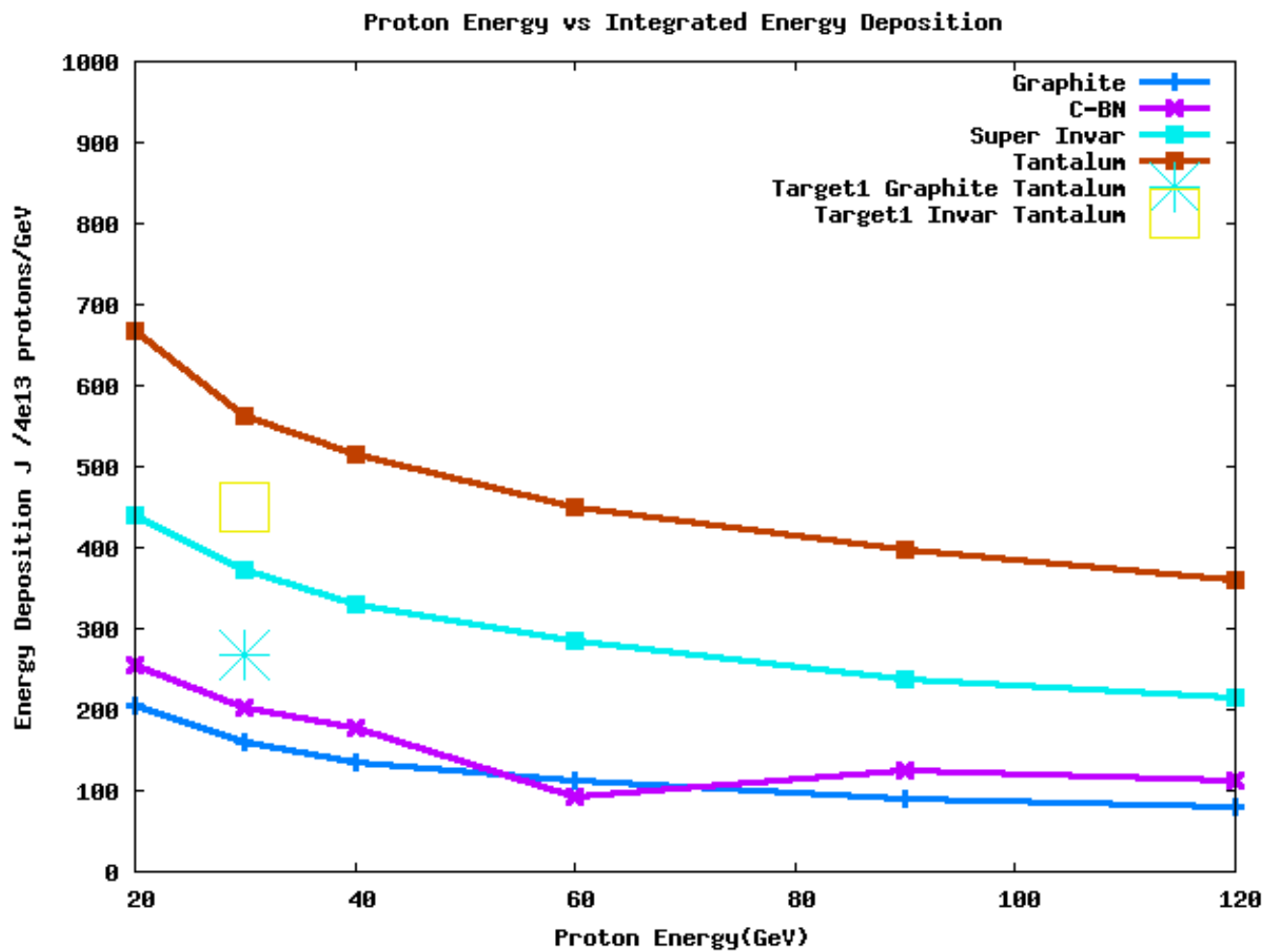


Figure 21: Integrated energy deposition (GeV/proton/ E_p) in cylindrical targets vs primary proton beam energy for different materials.

A.2 Decay Pipe Shielding

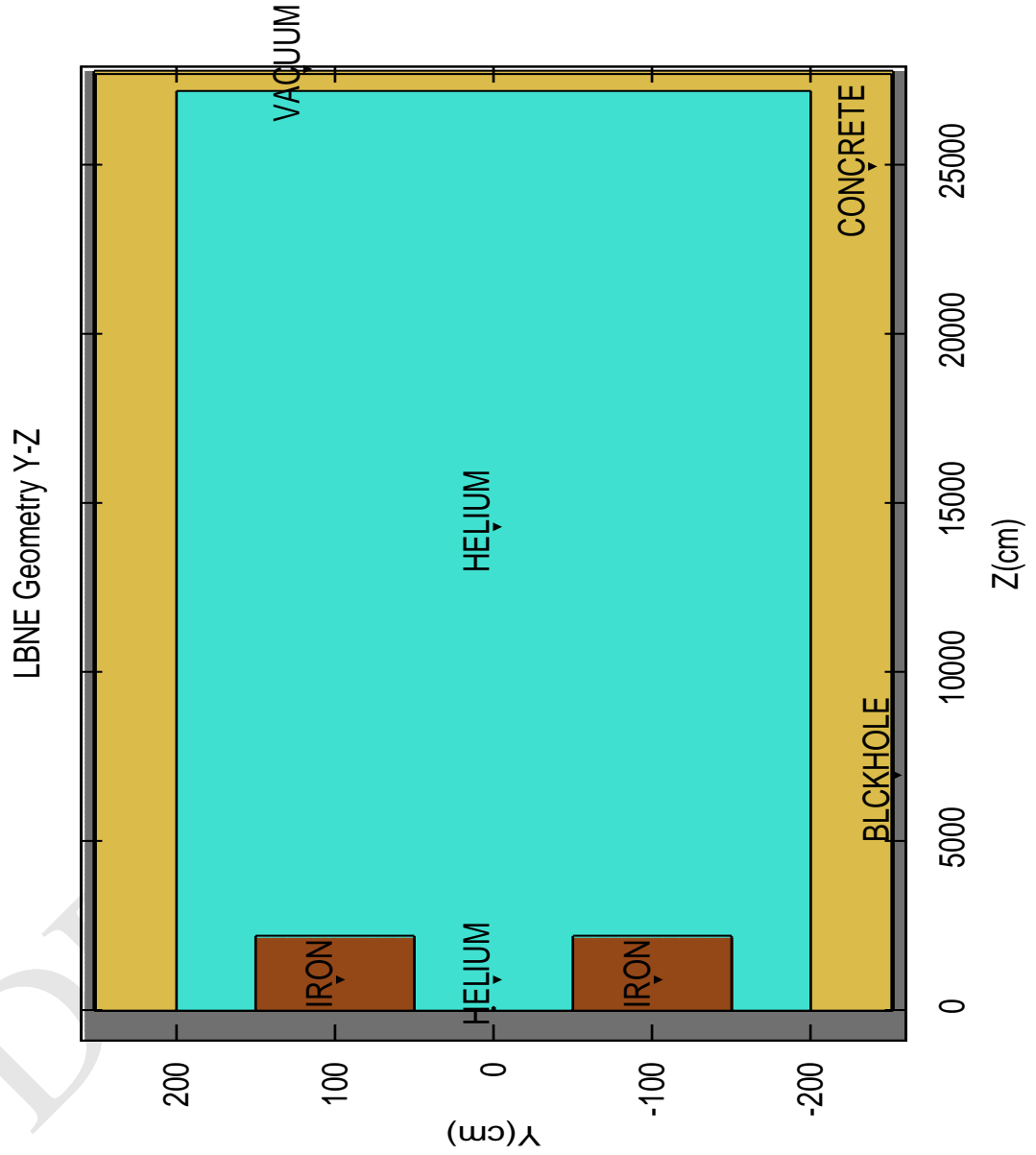


Figure 22: Simplified LBNE target and decay pipe shielding geometry simulated in FLUKA08. A graphite target of radius 0.6cm and 2 interaction lengths is located at 0,0,0. The proton beam is incident from the left

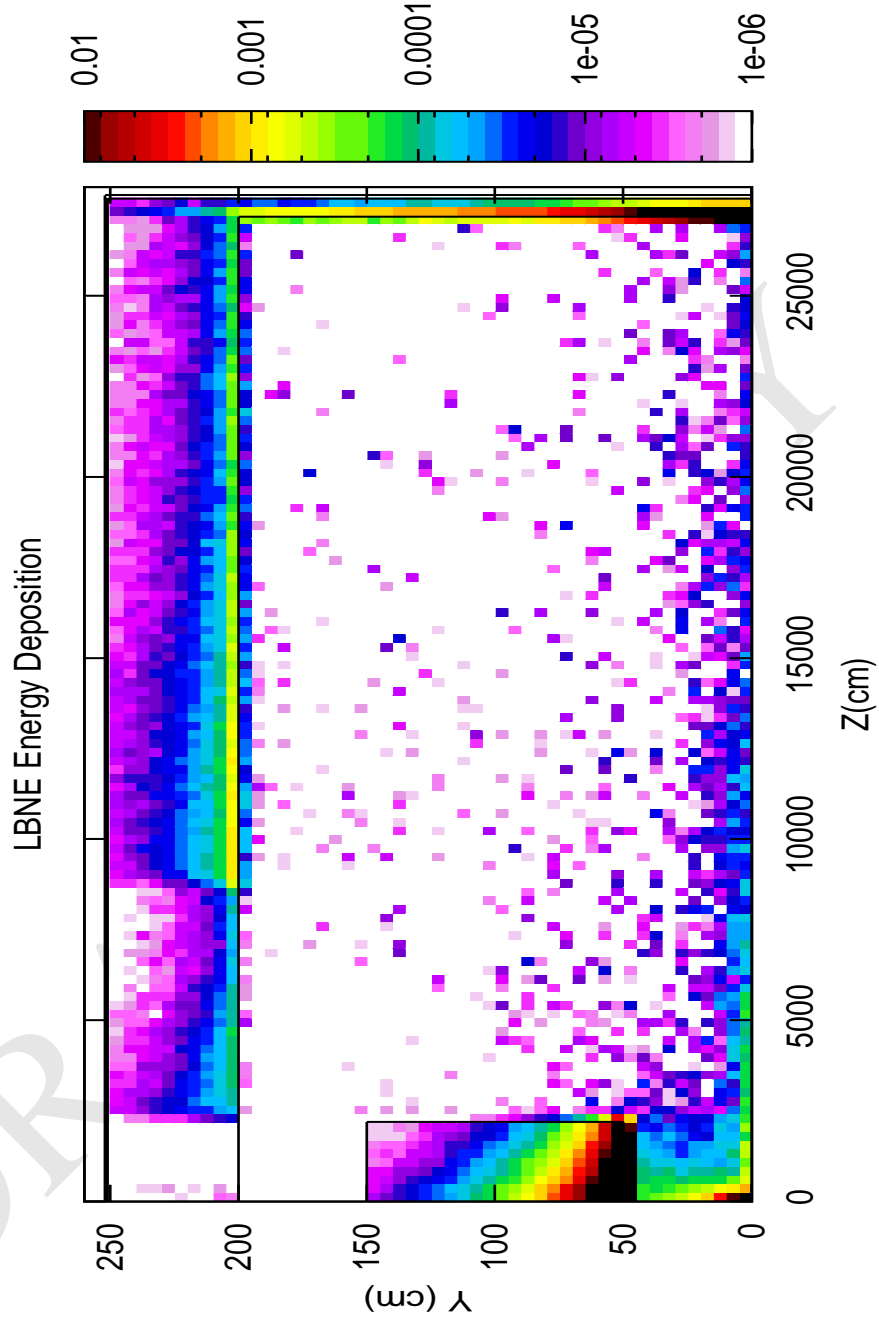


Figure 23: Energy deposition in the concrete shielding of a cylindrical 2m radius 250m long decay pipe. A proton beam of 30 GeV is incident from the left on a graphite target of 2 interaction lengths located at $z=0$ m. The decay pipe is filled with He at 1atm. There are no focusing elements included in this simulation. The energy density is given in units of Joules/ $16e13$ protons/ cm^3 .

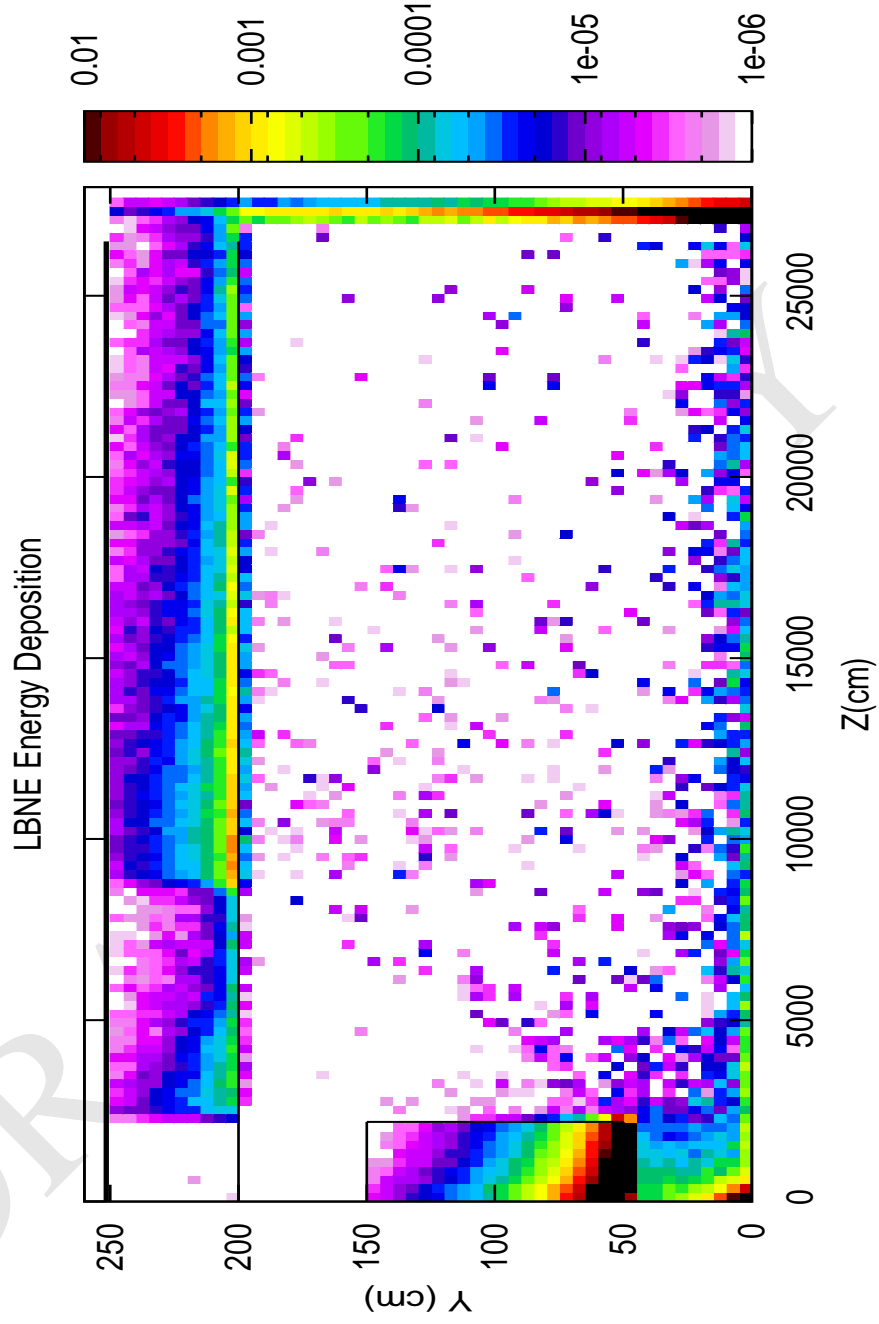


Figure 24: Energy deposition in the concrete shielding of a cylindrical 2m radius 250m long decay pipe. A proton beam of 60 GeV is incident from the left on a graphite target of 2 interaction lengths located at $z=0$ m. The decay pipe is filled with He at 1atm. There are no focusing elements included in this simulation. The energy density is given in units of Joules/ $8e13$ protons/ cm^3 .

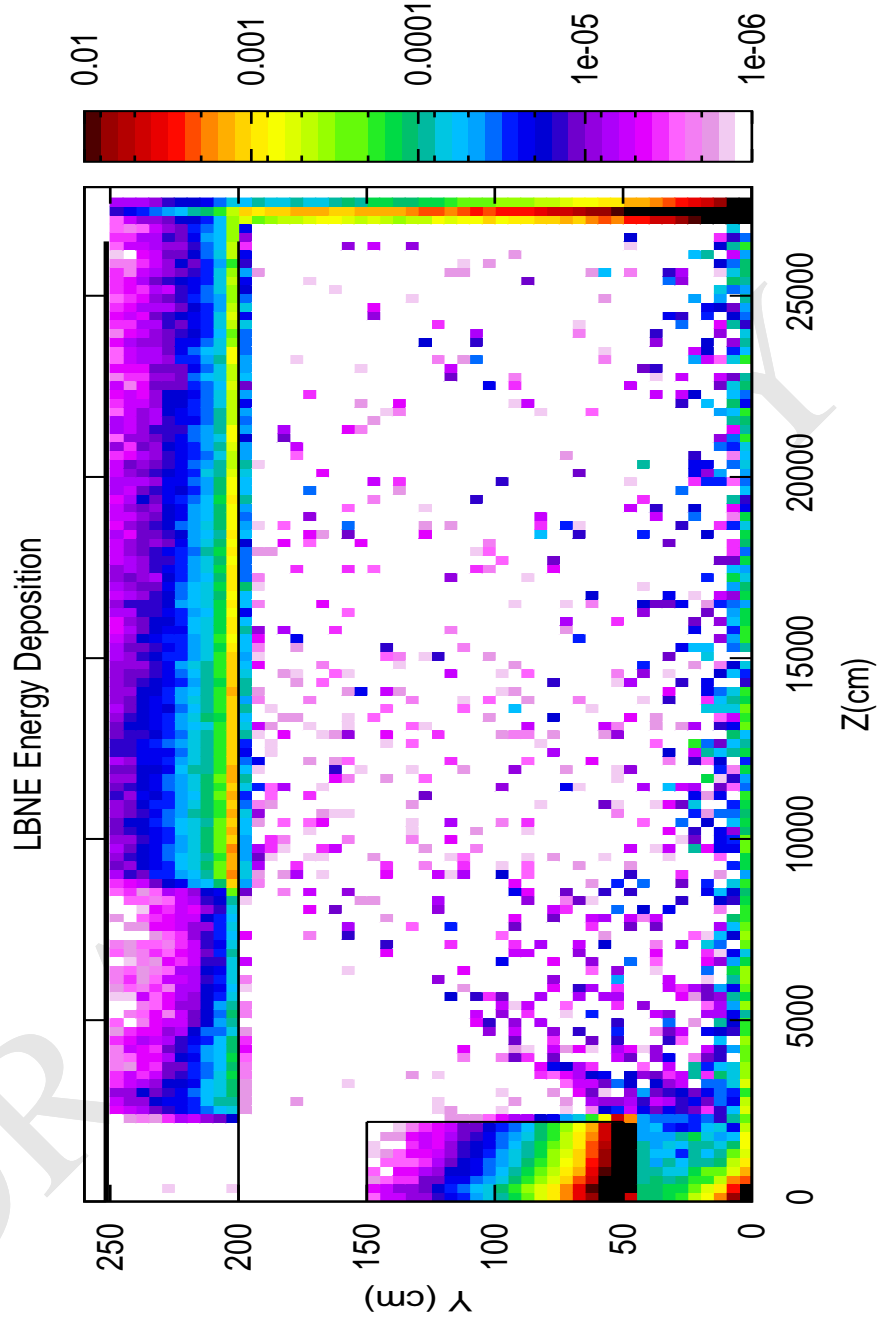


Figure 25: Energy deposition in the concrete shielding of a cylindrical 2m radius 250m long decay pipe. A proton beam of 120 GeV is incident from the left on a graphite target of 2 interaction lengths located at $z=0$ m. The decay pipe is filled with He at 1atm. There are no focusing elements included in this simulation. The energy density is given in units of Joules/ $4e13$ protons/ cm^3 .

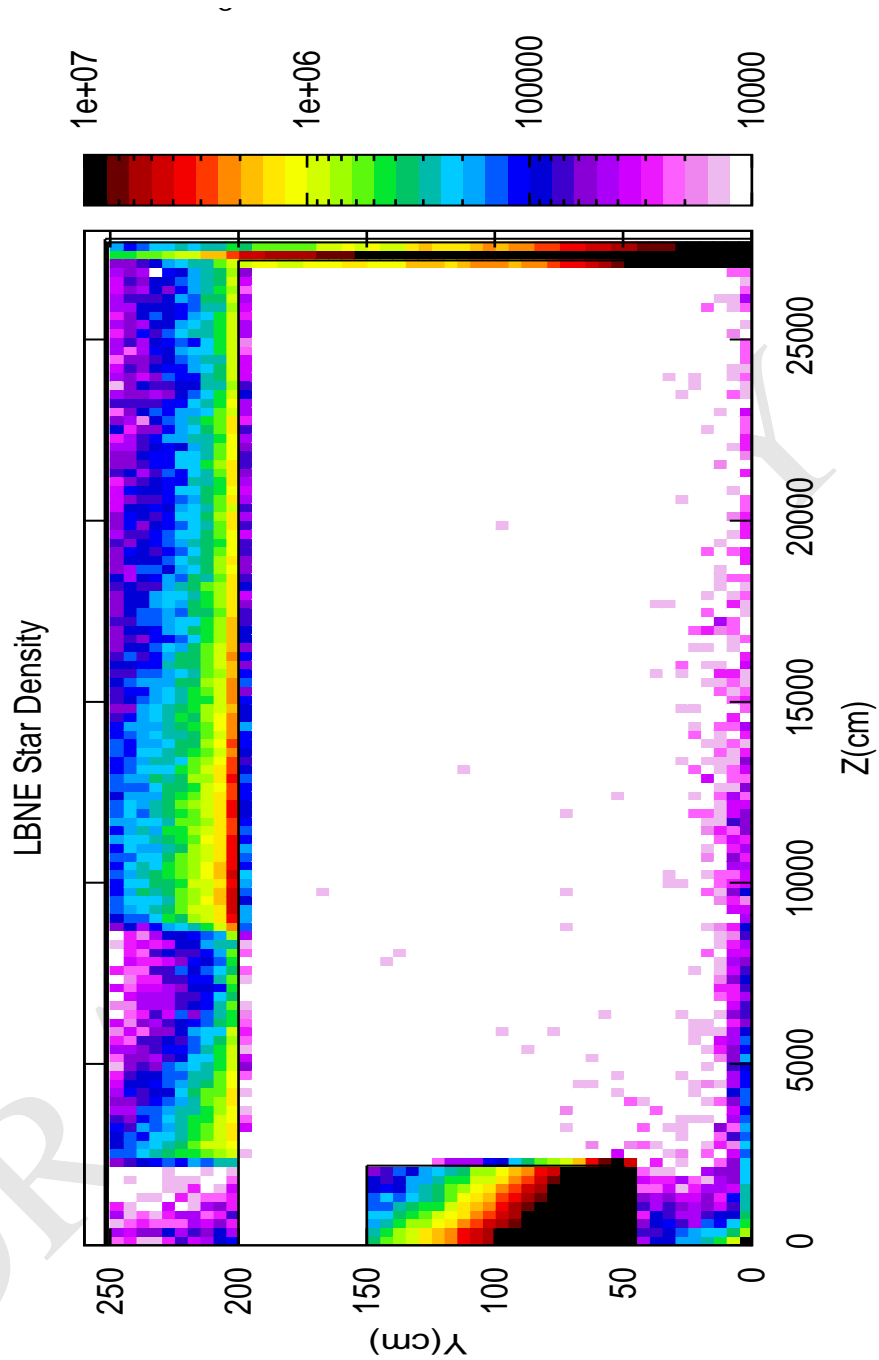


Figure 26: Star (inelastic interaction) density in the concrete shielding of a cylindrical 2m radius 250m long decay pipe. A proton beam of 30 GeV is incident from the left on a graphite target of 2 interaction lengths located at $z=0$ m. The decay pipe is filled with He at 1atm. There are no focusing elements included in this simulation. The star density is given in units of Stars/ $16e13$ protons/ cm^3 .

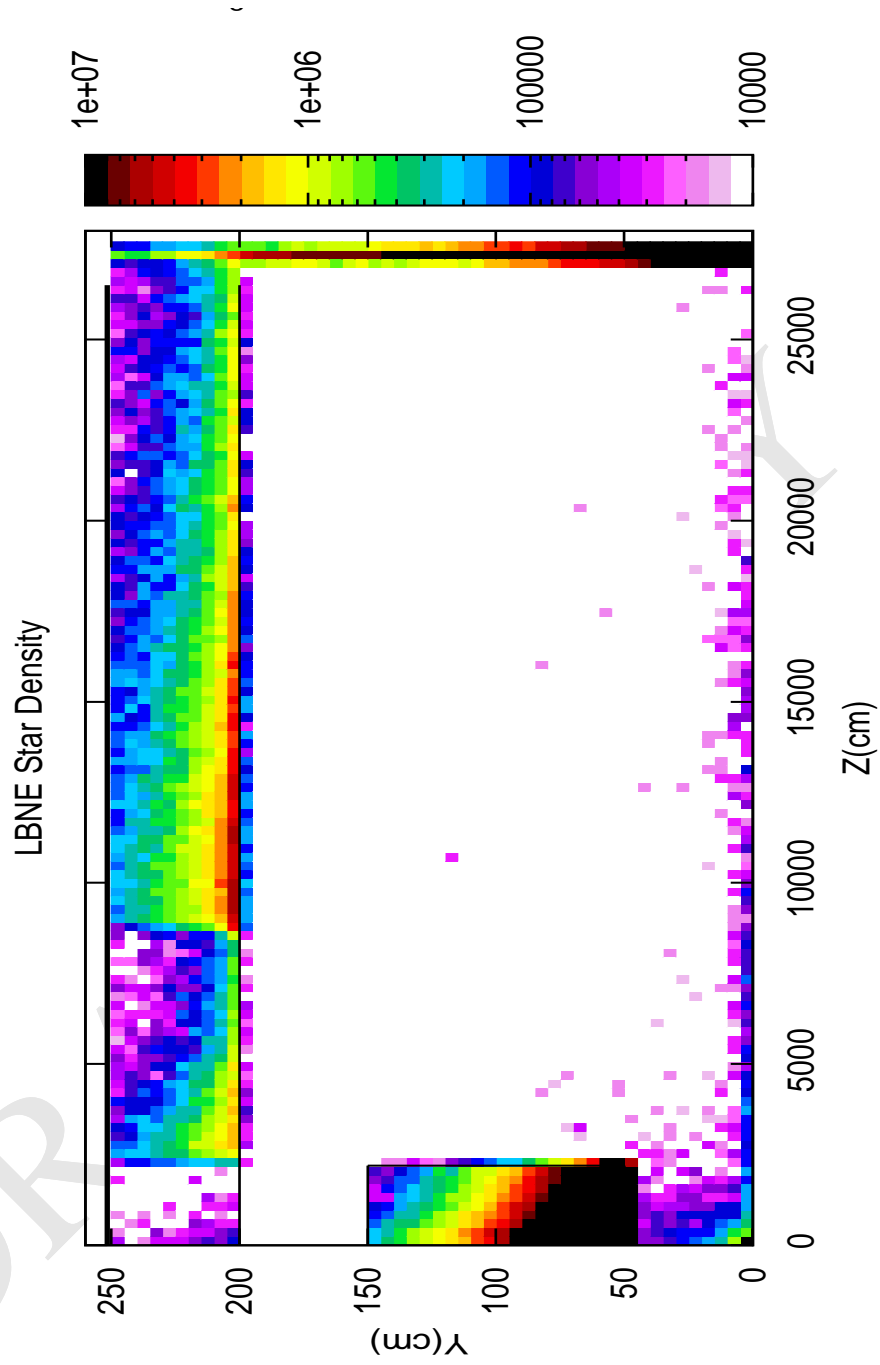


Figure 27: Star (inelastic interaction) density in the concrete shielding of a cylindrical 2m radius 250m long decay pipe. A proton beam of 60 GeV is incident from the left on a graphite target of 2 interaction lengths located at $z=0$ m. The decay pipe is filled with He at 1atm. There are no focusing elements included in this simulation. The star density is given in units of Stars/ $8e13$ protons/ cm^3 .

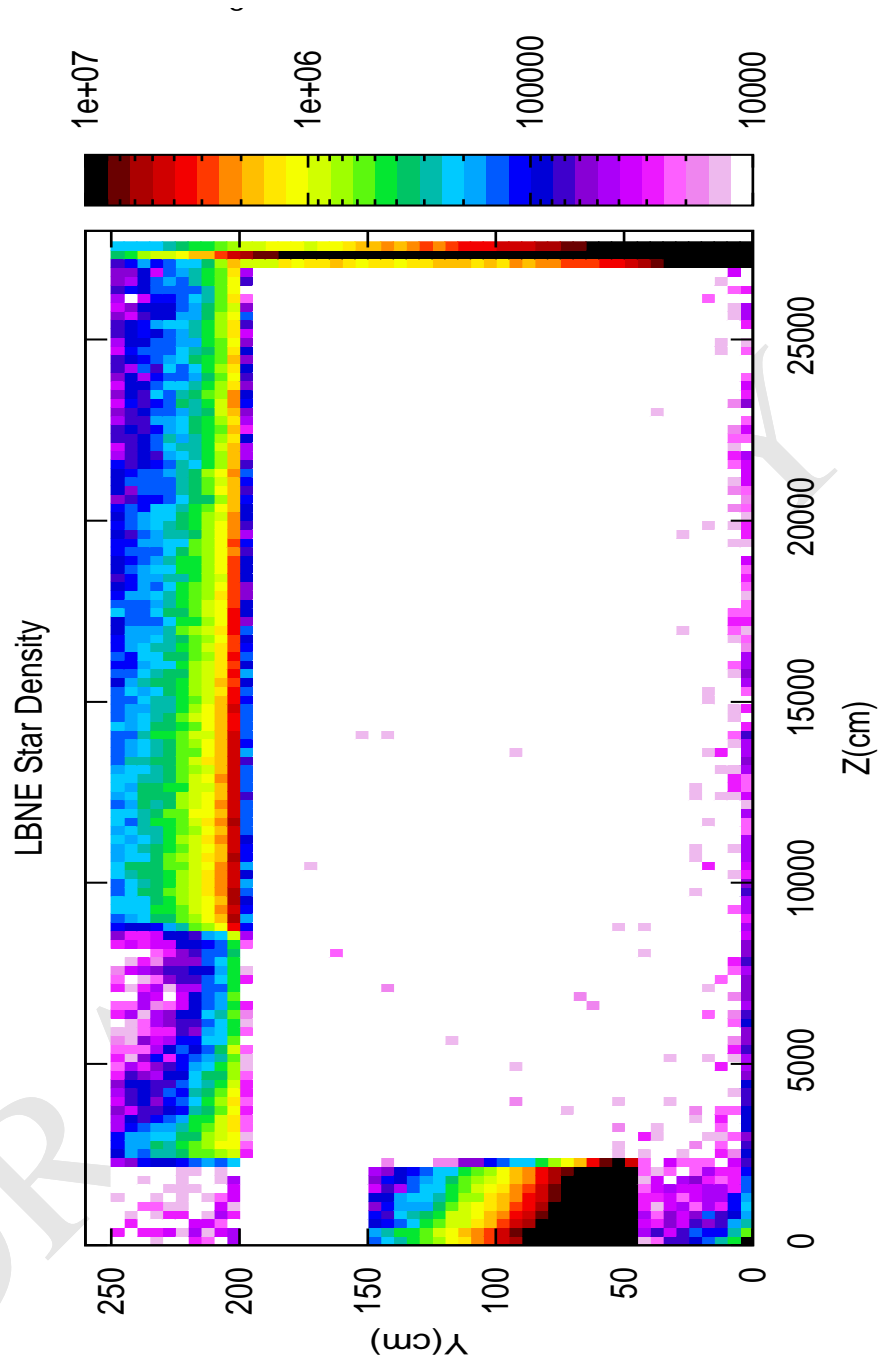


Figure 28: Star (inelastic interaction) density in the concrete shielding of a cylindrical 2m radius 250m long decay pipe. A proton beam of 120 GeV is incident from the left on a graphite target of 2 interaction lengths located at $z=0$ m. The decay pipe is filled with He at 1atm. There are no focusing elements included in this simulation. The star density is given in units of Stars/ $4e13$ protons/ cm^3 .

B FNAL MI Beam Power vs Energy

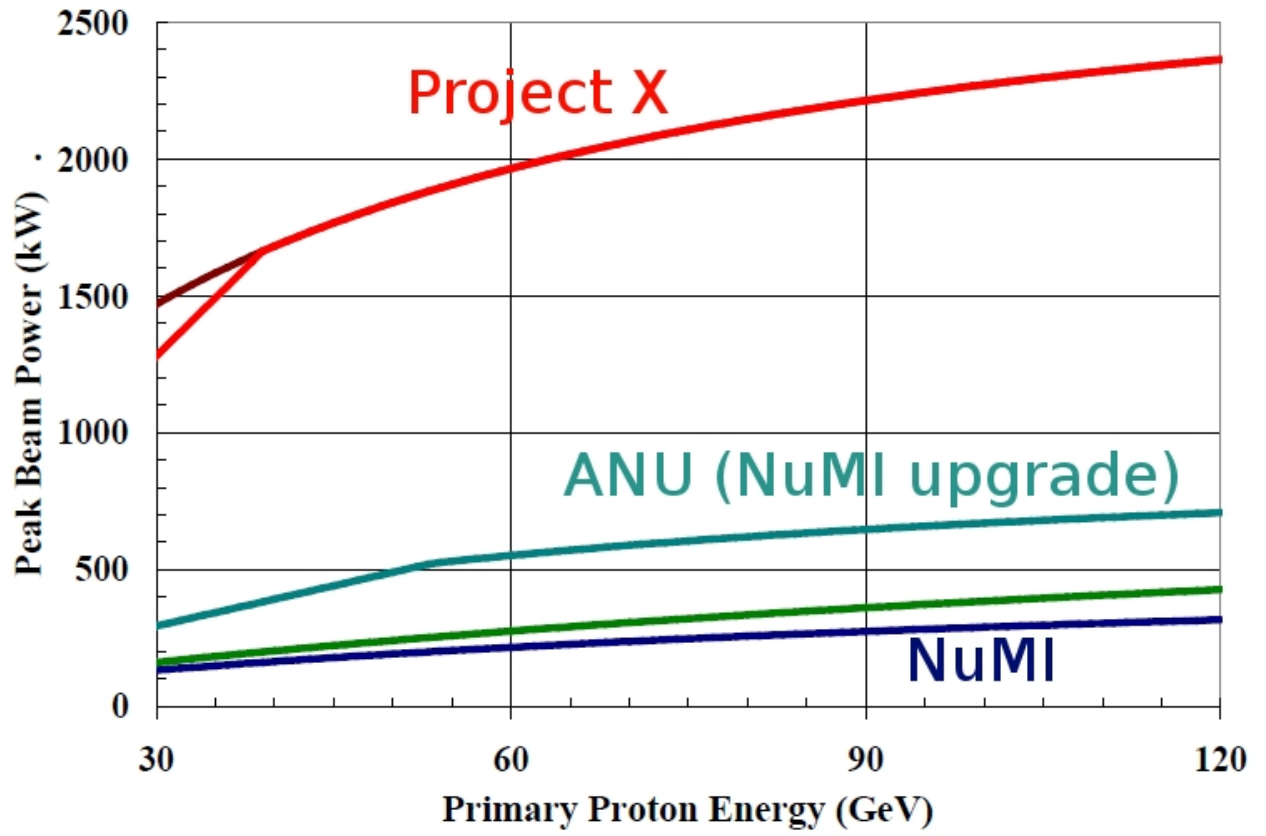


Figure 29: FNAL MI Beam power as a function of primary proton beam energy for various upgrade options. (Bob Zwaska)

C BNL-AGS vs FNAL-MI LBNE Beams

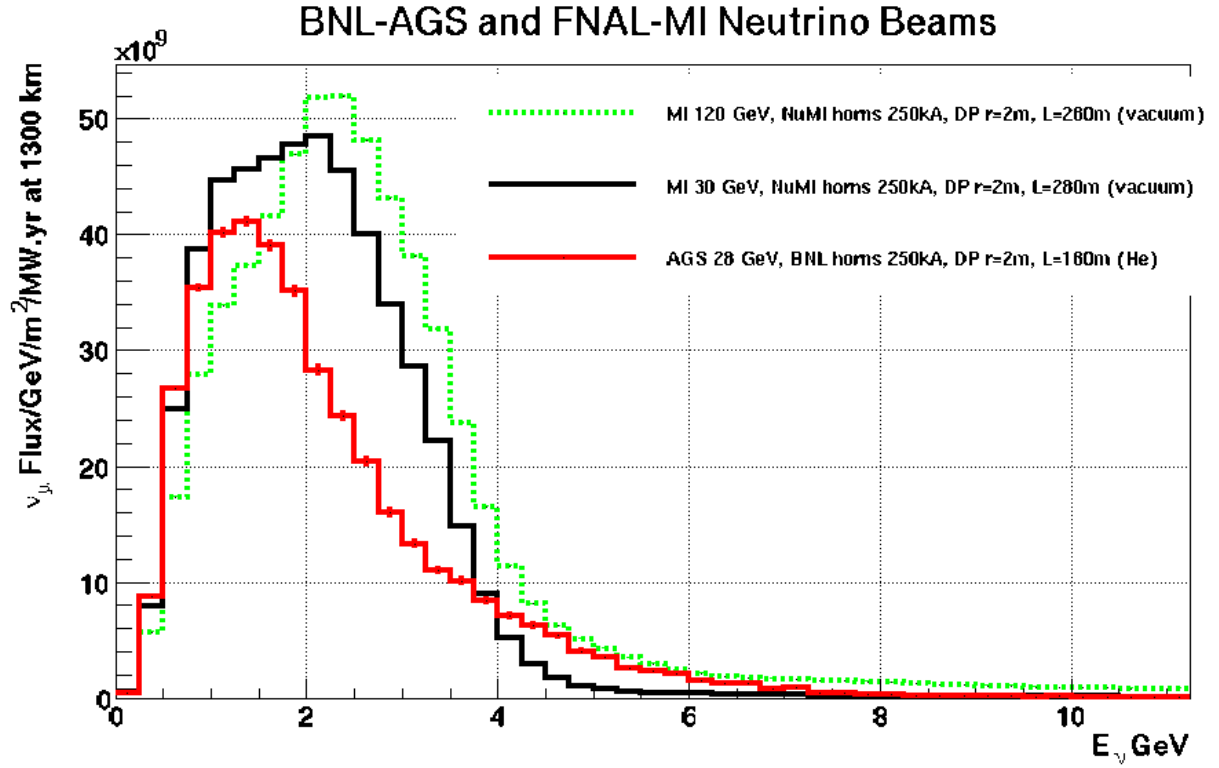


Figure 30: Neutrino flux from the BNL-AGS beam design as compared to the NuMI based MI designs at 30 and 120 GeV. All simulations used the FLUKA05-08/GEANT 3.21 based GNUMI framework and the flux is correctly extrapolated to the far detector. The target simulated is identical in both designs: high density graphite $r=0.6\text{cm}$ and 2 interaction lengths.